Guidelines for the synthesis of molybdenum nitride: Understanding the mechanism and the control of crystallographic phase and nitrogen content

Aleksandra Lilić, Luis Cardenas, Adel Mesbah, Erik Bonjour, Patrick Jame, Carine Michel, Stéphane Loridant, Noémie Perret

Guidelines for the synthesis of molybdenum nitride: understanding the mechanism and the control of crystallographic phase and nitrogen content

Aleksandra Lilić,[1,3] Luis Cardenas,[1] Adel Mesbah,[1] Erik Bonjour,[2] Patrick Jame,[2] Carine Michel,[3] Stéphane Loridant,[1] Noémie Perret[1*]

[1] Univ Lyon, Université Claude Bernard Lyon 1, CNRS, IRCELYON, F-*69626, Villeurbanne, France.*

[2] Univ Lyon, Université Claude Bernard Lyon 1, CNRS UMR 5280, *ISA, 69100 Villeurbanne, France.*

[3] Univ Lyon, ENS de Lyon, Laboratoire de Chimie, CNRS UMR 5182, Université Claude Bernard Lyon 1, *69342 Lyon, France.*

*corresponding author: noemie.perret@ircelyon.univ-lyon1.fr

Abstract

Bulk (Mo_2N) and supported molybdenum nitride (Mo_2N/TiO_2, Mo_2N/CeO_2) were synthesized by reduction-nitridation of bulk and supported MoO_3 under a mixture of N_2/H_2. We investigated the mechanism of formation of molybdenum nitrides by coupling elemental analysis, *in situ* and *ex situ* XRD, Raman spectroscopy, *in situ* XPS/UPS spectroscopy and DFT calculation. We showed that it is possible to control the crystallographic phase and degree of nitridation (i.e. nitrogen vacancies) by adjusting the parameters of the synthesis, including the heating rate and final temperature, the nature, composition and flow of gas during reduction/nitridation and cooling. We demonstrated that β-Mo_2N and γ-Mo_2N go through the same intermediates: molybdenum bronze, MoO_2 and Mo. The final crystallographic phase of the nitride depends mainly on the temperature rate and gas hourly space velocity employed during the synthesis, as they impact the crystallite size of the intermediates and the kinetics of reduction and nitridation. Molybdenum nitride clusters (< 0.5 nm) are formed on TiO_2.

Keywords

Nitride materials. Interstitial alloys. Clusters. Gas-solid reactions. Vacancy formation. Photoelectron spectroscopies.

1. Introduction

Molybdenum nitrides are obtained by interstitial incorporation of nitrogen into the lattice of metallic Mo resulting in modification of electron density and d-band contraction [1,2]. These materials display interesting properties such as good thermal and chemical stability, high hardness, high wear resistance, high melting points, low compressibility, magnetic and superconducting properties [3–6]. Therefore, they find application as superconductors [3,7], functional coatings [4,5], electrocatalyst in batteries and fuel cells [8–10] and heterogeneous catalysts [1,11,12].

Molybdenum nitride catalysts can exhibit similar catalytic activity and distinct selectivity response when compared with conventional metal catalysts. The nature of the active sites is still under debate, depending on the reaction. Nevertheless, there is a general consensus that the active sites are associated with Mo atoms and/or nitrogen deficient sites [13–16]. The nitrogen vacancies are favorable for the adsorption and dissociation of substrates. The catalytic property is linked in particular to the crystallographic phase [13,16–18], the size [19–22], Mo oxidation states [23,24], the degree of nitridation [14,25–27] and the passivation [28]. A fine control of these parameters would allow to tune the activity of the materials.

This work focuses on the two main allotropic forms of molybdenum nitride: tetragonal β-Mo_2N with N atoms in the tetrahedral interstitial sites and face center cubic γ-Mo_2N with N atoms occupying randomly half of the octahedral interstitial sites. The latter structure has been more widely studied by experimental and theoretical studies. A well-known method for their preparations is the temperature programmed reduction-nitridation (TPN) by gas-solid reaction of MoO_3 (or other Mo-containing precursor) with a mixture of N_2/H_2 or NH_3, under a thermal treatment.

Syntheses with NH_3 have been extensively studied; they generate γ-Mo_2N where some heat transfer problems have been reported due to the endothermic decomposition of NH_3 [29]. In 1994, it was shown for the first time [30] that γ-Mo_2N could be obtained by employing a mixture of N_2/H_2 instead of NH_3. A few years later, the formation of β-Mo_2N was also reported with this mixture [31]. TPN with N_2/H_2 gas mixture is advantageous because molybdenum nitride with varied crystallographic phase (β and γ) and textural properties can be synthesized by adjusting the reaction parameters such as the gas composition (i.e. N_2/H_2 ratio), heating rate (T_{rate} = 0.1-10 °C min^{-1}), final nitridation temperature (T_{max} = 500-800 °C), isothermal hold at final temperature, gas hourly space velocity (GHSV), and cooling gas choice (Ar, N_2, N_2/H_2) [13,17,30–32].

It was shown that the synthesis of the β-phase with N_2/H_2 goes through formation of MoO_2 and Mo metallic as intermediates [31,33–35]. The formation of a molybdenum bronze H_xMoO_3 intermediate was reported when some amount of Pd is added during the synthesis [36]. The mechanism of γ-Mo_2N

is hardly documented. Wise and Markel reported MoO_2 and an unidentified phase as intermediate [30]. They also proposed the formation of metallic Mo based on thermodynamic calculation, but without formal observation. It was also suggested [13] that γ-Mo_2N should follow the path MoO_3 > MoO_yN_{1-y} > γ-Mo_2N based on the literature employing NH_3 [37].

Part of the discrepancies observed so far is due to the fact that Mo_2N materials are often characterized after air exposure (*ex situ*) [38]. In this context, the investigation of the materials properties requires an in-depth characterization under *in situ* conditions. This paper introduces a new metodology to determine the structural, textural and electronic properties of the material during each stage of Mo_2N synthesis, passing through the oxidation of ammonium heptamolybdate tetrahydrate (AHM) $(NH_4)_6Mo_7O_{24}$ precursor and its subsequent oxidation followed by reduction/nitridation.

To increase the number of exposed sites, supporting small particles of Mo_2N appears as an appealing strategy. However, the literature dealing with the synthesis of supported nitrides is limited. These studies focus mainly on the catalytic application of the nitride systems and little work has been done on the optimization of the synthesis routes. This is partially due to the fact that the characterization of supported nanoparticles (e.g. crystallographic structure) is often more challenging than for bulk materials. Until now the synthesis of molybdenum nitride by impregnation with AHM followed by TPN with N_2/H_2 has been conducted on Al_2O_3 [18,39,40], SBA-15 [18] and activated carbon [20]. In this study, we explore the use of TiO_2 and CeO_2.

Understanding the elementary steps occurring during the synthesis of Mo_2N is a fundamental challenge for determining the final composition and crystallographic phase of the materials. Clarification of the synthesis mechanisms is needed to identify the important factors that controls the synthesis of the β and γ-phase for TPN with N_2/H_2. This mechanistic understanding needs to be based on solid experimental proofs of intermediate phases coupling *ex situ* and *in situ* characterizations. In this paper, we set out to examine how some critical properties, such as the quantity of N-deficient sites, can be tuned for β and γ-Mo_2N, depending on the synthesis conditions. Therefore, we are reporting the influence of heating rate (T_{rate}), final nitridation temperature (T_{max}), N_2/H_2 feed composition, GHSV and choice of the cooling gas on the formation of β or γ-phase. Mechanism of synthesis is revealed using Raman spectroscopy, *in situ* and *ex situ* X-ray, and *in situ* XPS/UPS. Finally, the syntheses of Mo_2N/TiO_2 and Mo_2N/CeO_2 are investigated and optimized.

2. Material and methods

2.1. Sample preparation

2.1.1. Bulk samples

Calcination of ammonium heptamolybdate tetrahydrate (AHM: $(NH_4)_6Mo_7O_{24}\cdot 4H_2O$; Sigma-Aldrich, 99.98% trace metal basis, XRD diffractogram shown in Supplementary material, Figure A.1a) in air flow (60 mL min^{-1}) at 350 °C (5 °C min^{-1}; hold for 2 h) gave MoO_3-AHM-350. This material was further used as MoO_3 precursor for the synthesis of bulk molybdenum nitrides by temperature programed reduction-nitridation (TPN). Between 1.1 g and 3.0 g of MoO_3-AHM-350 was packed onto a glass frit in a quartz synthesis reactor and placed in a vertical tube furnace. TPN was conducted under N_2/H_2 mixture (15%/85% or 85%/15% v/v) or NH_3 with a GHSV value of 87 min^{-1}, 109 min^{-1} or 230 min^{-1}. The temperature was increased by applying temperature rate (T_{rate}) of 5 or 0.5 °C min^{-1} until reaching the final nitridation temperature (T_{max} = 350−700 °C) and held for 2 h. Samples were cooled down to room temperature under nitrogen or argon flow (60 mL min^{-1}). Finally, the materials were passivated at room temperature during 4 h in 1% v/v O_2/N_2 flow (60 mL min^{-1}).

In standard condition (Mo_2N-5, Mo_2N-0.5), TPN was conducted under 15% v/v N_2/H_2 mixture with a GHSV value of 230 min^{-1} until 700 °C, and cooled down under nitrogen. The samples (Table 1) are labelled Mo_2N-5-X when T_{rate} = 5 °C min^{-1} and Mo_2N-0.5-X when T_{rate} = 0.5 °C min^{-1}. X refers to the main parameter varied during the synthesis: X = NH_3 or 85%N_2 when TPN was conducted under NH_3 or N_2/H_2 mixture with high nitrogen content (85% v/v N_2/H_2); X = T650 when the final temperature of TPN was 650 °C; X = GHSV-87 or GHSV-109 when a GHSV value of 87 min^{-1} or 109 min^{-1} was employed; X = Cool-Ar when the cooling down was conducted in Ar. The samples obtained are labelled with X = 63µ, 80µ or 315µ (Table 2), when MoO_3-AHM-350 was sieved and divided in 3 batches (40-63 µm, 63-80 µm and 100-315 µm) before TPN in standard condition.

Calcination of AHM in air flow (60 mL min^{-1}) at 700 °C (5 °C min^{-1}; hold for 2 h) gave MoO_3-AHM-700. This material was used for the synthesis of molybdenum nitride employing the standard condition of TPN (Table 3).

MoO_3-5-T350-H_2 and MoO_3-0.5-T350-H_2 were synthesized from MoO_3-AHM-350. The reductions were conducted under H_2 with a GHSV 230 min^{-1}. The temperature was increased at T_{rate} (5 or 0.5 °C min^{-1}) until 350 °C and held for 2 h. the samples were cooled down under Ar.

Mo-5 and Mo-0.5 (Table A.1) were synthesized from MoO_3-AHM-350. The reductions were conducted under H_2 with a GHSV 230 min^{-1}. The temperature was increased at T_{rate} (5 or 0.5 °C min^{-1}) until 700 °C and held for 2 h. Samples were cooled down to room temperature under argon flow (60 mL min^{-1}). The samples were either passivated at room temperature for *ex situ* analyses, or re-used

directly *in situ* for the syntheses of Mo_2N-5-Mo and Mo_2N-0.5-Mo (Table A.1). In the latter case, TPN were conducted in standard condition under N_2/H_2 mixture (15% v/v) with a GHSV of 230 min^{-1}. The temperature was increased by applying T_{rate} of 5 or 0.5 °C min^{-1} until 700 °C and held for 2 h. Samples were cooled down to room temperature under nitrogen flow and passivated, as previously.

2.1.2. Supported samples

Supported samples were prepared by impregnation of AHM followed by temperature programmed reduction-nitridation. The supports used were commercial powders of DT51D TiO_2 (Tronox), and HSA 5 CeO_2 (Solvay Rhodia). First, the supports were calcined under Ar at 700 °C for 2 h (5 °C min^{-1}). Their specific surface areas diminished after calcination: from 91 to 48 $m^2 g^{-1}$ for TiO_2 and from 289 to 109 $m^2 g^{-1}$ for CeO_2. The precursors, AHM/TiO_2 and AHM/CeO_2, were synthesized by aqueous wet impregnation of AHM (1 g in 60 mL of H_2O; corresponding to 9.8 wt% Mo) on support (5 g) followed by stirring at room temperature for 2 h, water evaporation using rotavapor evaporator and by drying in an oven at 80 °C under N_2 flow overnight. MoO_3/TiO_2, and MoO_3/CeO_2 were obtained by calcination of the precursors under air at 350 °C for 2 h (5 °C min^{-1}). About 1.1 g of MoO_3/support was packed onto a glass frit in a quartz synthesis reactor and placed in a vertical tube furnace. TPN was conducted under 15% v/v N_2/H_2 (GHSV 230 min^{-1}). The temperature was increased by applying temperature rate (T_{rate} of 5 or 0.5 °C min^{-1}) until reaching the final temperature (T_{max} = 500 °C, 600 °C, or 700 °C) and held at T_{max} for a specific time (iso = 2 or 24 h). Samples were cooled down to room temperature under nitrogen flow and passivated, as previously. The samples are labeled Mo_2N/TiO_2 (T_{rate}-T_{max}-iso) and Mo_2N/CeO_2 (T_{rate}-T_{max}-iso).

2.2. Characterization

A Bruker D8 Advance 25 X-ray diffractometer equipped with a Cu Kα radiation source (λ = 1.54184 Å) was used to record X-ray diffraction (XRD) patterns in the range 2θ = 5−100 ° at 0.04 ° s^{-1}. Phase identification was performed using the DiffracSuite Eva software (Bruker) and the JCPDS-ICDD-PDF4+ database. Lattice parameters, mean crystallite sizes (d=4/3 * LVol-IB; with LVol-IB the volume averaged column height) and phases quantification (wt%) were obtained by performing Rietveld refinements using either Topas 5 or FullProf programs. *In situ* XRD analysis on bulk MoO_3-AHM-350 under 15% v/v N_2/H_2 (5 °C min^{-1}) was performed from 25 to 700 °C using a D8-Advance BRUKER X-ray diffractometer with Bragg-Brentano Theta-Theta geometry equipped with an Anton Paar XRK-900 reactor chamber.

Brunauer−Emmett−Teller specific surface areas (S_{BET}) were determined by low temperature nitrogen physisorption performed at -196 °C, on a Micromeritics ASAP 2020 apparatus, after a 3 h

pretreatment under vacuum (10^{-7} bar) at 350 °C. The values are reported with an absolute accuracy of ± 5 m^2 g^{-1}.

Quantification of hydrogen present in the solids was performed using a homemade carbon-hydrogen micro-analyser (CNRS ISA, Villeurbanne, France). Sample weighted from 3 to 5 mg in silver capsules were dropped into a unit combustion hold at 1050 °C in a flow of 50 mL min^{-1} of O_2 followed by a second oven filled with copper oxide. Hydrogen was converted into H_2O quantified using a non-dispersive H_2O infra-red detector Rosemount NGA 2000. Nitrogen was analyzed using a similar homemade micro-analyzer (CNRS ISA, Villeurbanne, France) according to the Dumas method. Sample weighted in the same silver cup were dropped in the same unit combustion system in a flow of He (40 mL min^{-1}) added with O_2 (2 mL min^{-1}). The carbon, hydrogen and nitrogen elements were converted into carbon dioxide, water and nitrogen oxides. The later ones were reduced in nitrogen on copper maintained at 450 °C and the excess of oxygen was also trapped. Carbon dioxide and water were retained using an ascarite (sodium hydroxide-coated silica)-magnesium perchlorate trap. Nitrogen was quantified using a Thermo Conductibility Detector. Hydrogen and nitrogen percentages were calculated via linear calibrations prepared with high purity standards. Potassium biphtalate (%H: 2.47, Leco corp), Uracil (%H: 3.60) Phtalic acid (%H: 3.64) Acetanilide (%N: 10.36) O-phospho-DL-serine (%N: 4.56) all Sigma Aldrich and 502- 308 (%N: 0.20) and 502-309 (%N: 1.03) both Leco corp. The uncertainty of hydrogen and nitrogen elements are ± 0.10% in the range (0-3%) and ± 0.20% for nitrogen values in the range from 3 to 7%. The stoichiometry x of Mo_2N_x is given with an uncertainty ± 0.02.

Carbon contents were determined using Inductar Carbon Sulfur Cube (Elementar GmbH, Langenselbold, Germany) elemental analyzer. About 15 mg of sample weighted in nickel capsules (Lüdiswiss, Flawil, Switzerland) was placed in ceramic crucibles added with W/Sn as accelerators of combustion. Afterward the ceramic crucible was introduced in the induction furnace in a flow of 190 mL min^{-1} of O_2. The carbon contained in the sample was transformed into CO_2 at temperature close to 2000 °C and quantified using a CO_2 non-dispersive infrared detector. Molybdenum carbide Mo_2C (5.89%) Sigma Aldrich was regularly measured as internal standard in the aim to verify a non-drift of the CS Cube Inductar calibration. Carbon uncertainty was evaluated to ± 0.10%.

The Mo content of the solid was determined by inductively coupled plasma optical emission spectroscopy (ICP-OES) by using an ACTIVA instrument (HORIBA Jobin Yvon). Before analysis, the samples were mineralized in a mixture of H_2SO_4 + HNO_3 + HF followed by evaporation and soaking in HNO_3. Mo uncertainty was evaluated to ± 0.10%.

Raman spectra were recorded at room temperature using a LabRam HR (Jobin Yvon–Horiba) spectrometer equipped with a CCD detector cooled at -76 °C. Measurements were carried out at room

temperature under a microscope with a 50x objective that focuses the laser beam on the sample surface and collects the scattered light. The exciting line at 514.53 nm of Ar^+ laser was used with a power limited at 100 microW. It was previously checked that the samples laser heating was negligible with such power. A 300 or 1800 grooves mm^{-1} grating was used to disperse light leading to band position accuracy within 4 or 0.5 cm^{-1}, respectively.

The thermogravimetric analyses (TGA) were performed on a SETARAM LABSYS instrument in the 25-700 °C temperature range, on 20-40 mg of sample, with a heating rate of 5 °C min^{-1}, under argon or air flow (50 mL min^{-1}). This technique was used to determine the optimal temperature of calcination and reduction, and to verify their thermal stability. Simultaneous thermogravimetric and differential thermal analyses (TG-DTA) of the samples were conducted on a SETARAM SETSYS Evolution 12 thermo-analyzer coupled via a heated (*ca*. 150 °C) capillary with a Pfeiffer OmniStar quadrupole mass spectrometer (MS). For TG-DTA-MS studies, ca. 20 mg of samples were heated from room temperature to 750 °C at a constant rate of 5 °C min^{-1} under 3% v/v H_2/Ar (50 mL min^{-1}).

In order to reveal morphology of the materials SEM images were obtained using ThermoFisher QUATTRO-S microscope with LVD (low-vacuum detector (SE)) and acceleration voltage of 20 kV. Transmission electron microscopy (TEM) and scanning TEM–high angle annular dark field (STEM-HAADF) images were obtained using an image-aberration-corrected FEI Titan ETEM G2 instrument operated at 300 kV, equipped with an XMAX SDD EDX detector from Oxford Instruments. Samples were prepared by dispersing the solids in ethanol and then depositing them onto carbon-coated copper grids.

Ultraviolet photoelectron spectroscopy (UPS) analysis was used to determine the electronic structure of the valence band of Mo polymorphs. Prior to measurements, Ag foil was cleaned by several cycles of 2 KeV Ar^+ sputtering at room temperature (RT). An aqueous solution of 4 mmol L^{-1} of AHM in water was used as a precursor. It was ultrasonically dispersed and subsequently injected at RT under vacuum conditions using the atomic liquid injection system (ALI). The ALI system was charged with the colloidal solution of AHM. The pressure of the load-lock chamber where ALI is installed has a vacuum > 10^{-6} Torr. The coating's quality and homogeneity are assured by tuning the spray injection conditions, such as injection pressure and obturator aperture pulses time. The ALI shutter time (required time for full valve open) was 40 ms, and the pressure reached after each aperture was $3x10^{-4}$ Torr. A pressure of 800 mbar of carrier gas (argon) was applied to inject the AHM into the chamber. Several injections of AHM were carried out on the conducting Ag foil previously cleaned. After each injection, the coating was analyzed by XPS.

UPS/XPS measurements were achieved in a commercial AXIS-ULTRA DLD spectrometer using an Al Kα (1486.6 eV) XPS source and a discharge UV lamp delivering photons at 21.2 eV,

corresponding to the He Iα line typically used in UPS. Under these conditions, the intrinsic spectral resolution was measured at the Fermi edge of the Ag foil at room temperature, and it was estimated to be 0.15 eV. For comparison, the intrinsic resolution of a lab-based XPS setup using a monochromatized source is more than 0.55 eV. The UP spectral background was corrected using a mathematical function developed by Li *et al*. [41] for UPS analysis and implemented later by Maheu *et al.* on TiO_2 nanopowders [42].

XPS analysis on Mo polymorphs revealed well-resolved core levels corresponding to Mo 3d, Mo 3p, N 1s, C 1s, and Ag 3d. Mo 3p and Mo 3d core levels were fitted using a combination of Voigt line shapes. For this study, AHM was systematically subjected to oxidative and nitriding treatments using a catalytic reactor cell connected *in situ* to the UPS/XPS analysis chamber under UHV, providing a direct sample transfer without contact with the air. AHM was exposed under 40 mL min^{-1} O_2 flow during 2 h at 250 °C and subsequently analyzed by UPS/XPS. The reduction-nitridation process was carried out on AHM previously oxidized (in order to form MoO_3) under 15% v/v N_2/H_2 flow (40 mL min^{-1}) at 5 °C min^{-1} up to 700 °C and hold for 3 h.

2.3. Computational details

Calculations were performed by applying the density functional theory (DFT) within the generalized gradient approximation (GGA) using the Perdew−Burke−Ernzerhof functional (GGA-PBE) [43] as implemented in the Vienna ab initio simulation package (VASP) [44,45]. The electron−ion interaction was described by the projector augmented wave (PAW) method [46,47]. The valence electron configurations of Mo, N and O atom were defined as ($4s^2$ $4p^6$ $5s^1$ $4d^5$), ($2s^2$ $2p^3$) and ($2s^2$ $2p^4$), respectively. All calculations were performed with the plane-wave cutoff energy of 600 eV and a gaussian smearing with a 0.05 eV width. The Brillouin-zone integrations used Monkhorst–Pack grids [48] with a mesh of 12 x 8 x 12 (for MoO_3), 11 x 11 x 11 (for Mo, and γ-Mo_2N), and 11 x 11 x 5 (for β-Mo_2N). Bulk geometries were optimized using a 10^{-5} eV convergence criterium on the electronic energy and 0.05 eV $Å^{-1}$ on the forces exerted on the atoms and the cell vectors (cell volume and shape are both optimized).

Density of states (DOS) were calculated for MoO_3, β-Mo_2N, and γ-Mo_2N. Our results agree with previously published works for β-Mo_2N, and γ-Mo_2N [49,50]. For MoO_3 good agreement is also obtained, but the value of the band gap on our DOS is inferior to experimental value of band gap (around 3 eV), as expected while using a GGA functional.[64,65,74,75] In order to compare spectra obtained by UPS with calculated DOS, cross-section (σ) weighting for corresponding UPS source (He I=21.2 eV) and Gaussian convolution (FWHM=0.2 eV) were applied to calculated DOS of MoO_3, β-Mo_2N, and γ-Mo_2N [51–54]. First, the intensities of O 2p, N 2p, Mo 5s, and Mo 4d partial DOSs are weighted

to the one-electron ionization cross-sections (σ) of 10.67 Mb, 9.699 Mb, 0.04 Mb, and 26.27 Mb, respectively, as found in tables reported by Yeh and Lindau [54] for 21.2 eV. Then, for each cross-section weighted total DOS, a Gaussian fitting by using FWHM=0.2 eV was performed.

3. Results and discussion

3.1. Molybdenum nitride

3.1.1. Effect of synthesis parameters on nitride phase and nitrogen content

Table 1. *Influence of gas composition, GHSV, heating rate (T_{rate}), temperature maximal (T_{max}) and cooling gas on Mo nitride structural properties.*

Sample name	*N_2/H_2 % v/v*	*GHSV (min^{-1})*	*T_{rate} (°C min^{-1})*	*T_{max} (°C)*[a]	*Cooling gas*	*Phases obtained (XRD)*	*S_{BET} (m^2 g^{-1})*	*N (wt%)*[b]	*Mo_2N_x (x)*[b]
Mo_2N-5	15	230	**5**	700	N_2	β-Mo_2N	16	6.5	0.95
Mo_2N-0.5	15	230	**0.5**	700	N_2	γ-Mo_2N	41	6.6	0.97
Mo_2N-0.5-NH_3	**NH_3**	230	0.5	700	N_2	γ-Mo_2N	125	9.5	1.44
Mo_2N-5-T650	15	230	5	**650**	N_2	β-Mo_2N	17	6.6	0.98
Mo_2N-0.5-T650	15	230	0.5	**650**	N_2	γ-Mo_2N	55	6.2	0.91
Mo_2N-5-Cool-Ar	15	230	5	700	**Ar**	Mo + β-Mo_2N	16	-	-
Mo_2N-0.5-Cool-Ar	15	230	0.5	700	**Ar**	Mo, β-Mo_2N + γ-Mo_2N	33	-	-
Mo_2N-5-GHSV-109	15	**109**	5	700	N_2	β-Mo_2N	16	6.4	0.92
Mo_2N-5-GHSV-87	15	**87**	5	700	N_2	β-Mo_2N	15	6.4	0.92
Mo_2N-0.5-GHSV-87	15	**87**	0.5	700	N_2	β-Mo_2N + γ-Mo_2N	16	-	-
Mo_2N-5-85%N_2	**85**	230	5	700	N_2	MoO_2 + Mo + β-Mo_2N	19	-	-
Mo_2N-0.5-85%N_2	**85**	230	0.5	700	N_2	β-Mo_2N + γ-Mo_2N	22	-	-

[a] *T_{max} is dwelled for 2 h;* [b] *based on elemental analysis (N ± 0.2%; x ± 0.02).*

First, some of the synthesis parameters of bulk molybdenum nitride were varied in order to elaborate Mo_2N with different crystallographic phases and nitrogen contents. For this purpose, a range of samples were synthesized by temperature programmed reduction-nitridation (TPN) of solid MoO_3 under a flow of N_2/H_2 followed by cooling under inert gas and passivation. MoO_3 was obtained by calcination of AHM under air at 350 °C (MoO_3-AHM-350). This solid exhibit an orthorhombic structure MoO_3 (XRD in Figure A.1b) and a specific surface area (S_{BET}) of 15 m^2 g^{-1}.

During the reduction/nitridation reaction of MoO_3 with N_2/H_2 gas mixture, the gas composition (15 or 85% v/v N_2/H_2), the GHSV value (87-230 min^{-1}), the heating rate T_{rate} (5 or 0.5 °C min^{-1}), the final temperature of nitridation (T_{max} = 650 or 700 °C), and the cooling gas (N_2 or Ar) were varied. Table 1 summarizes the crucial parameters of the syntheses, the crystallographic phases observed by XRD, the

specific surface areas, the nitrogen contents (N wt%) and stoichiometries of the synthesized samples. The XRD diffractograms associated with the samples are presented in Figure 1 and Figure A.2.

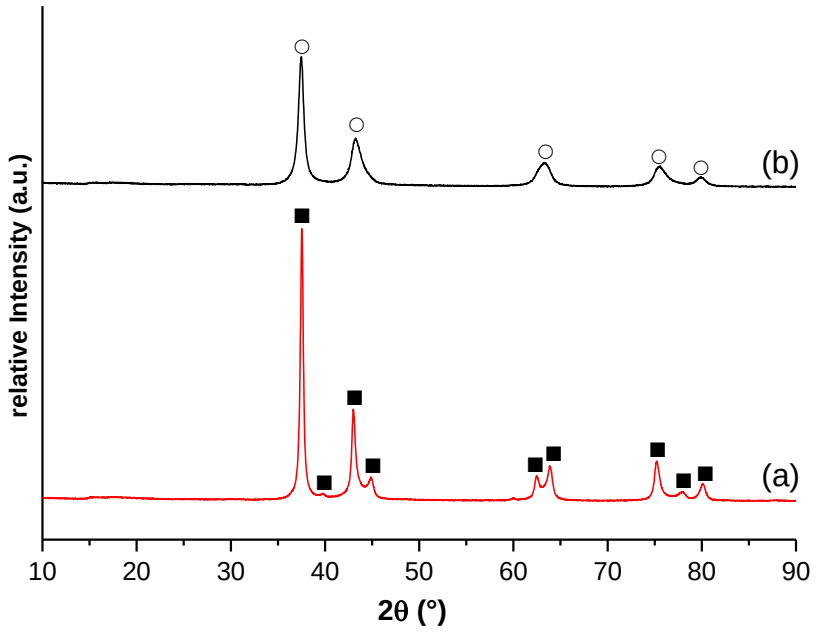

Figure 1. *XRD diffractograms of (a) Mo_2N-5 corresponding to β-Mo_2N, and (b) Mo_2N-0.5 corresponding to γ-Mo_2N. XRD peak assignments based on ICDD files: (■) β-Mo_2N (PDF 01-075-1150) and (○) γ-Mo_2N (PDF 00-025-1366).*

The first two samples were synthesized by TPN of MoO_3 with a flow of 15% v/v N_2/H_2 at a GHSV of 230 min^{-1} up to 700 °C. When the heating rate was 5 °C min^{-1}, pure tetragonal β-Mo_2N was obtained (Mo_2N-5, Table 1, Figure 1) with a mean crystallite size of 20 nm and a specific surface area of 16 m^2 g^{-1}. Based on the N wt% determined by elemental analysis, stoichiometric formula of this sample is $Mo_2N_{0.96}$. Pure fcc γ-Mo_2N with an average crystallite size of 10 nm and a Mo:N stoichiometry of 2:0.98 was formed using a heating rate of 0.5 °C min^{-1} (Mo_2N-0.5, Table 1, Figure 1). The diffractogram associated with β-Mo_2N (Figure 1-a) presents a tetragonal structure (space group I41/amd) with 9 main peaks at 37.7° (100%), 39.9° (3%), 43.0° (33%), 45.1° (9%), 62.5° (10%), 64.0° (13%), 75.3° (15%), 78.0° (4%) and 80.2° (7%). γ-Mo_2N presents a distinct diffractogram (Figure 1-b) with 5 main peaks at 37.4° (100%), 43.4° (36%), 63.1° (19%), 75.7° (15%) and 79.7° (8%) consistent with a cubic structure (space group Pm-3m). No additional peaks associated with other Mo phases such as oxides (MoO_3, MoO_2), Mo metal, or oxynitrides, were observed in the two diffractograms. Raman spectrum of β-Mo_2N and γ-Mo_2N are presented in Figure A.3. Since materials with metallic character are not active for Raman analysis, the flat signals confirm the absence of amorphous oxide phases and full nitridation. It is well accepted that passivation of molybdenum

nitrides with a flow of diluted O_2 (1%) in inert gas results in the formation of one or two chemisorbed oxygen layers [33]. Our results confirmed that the passivation step does not impair the results obtained by XRD and Raman spectroscopy, the analyses of crystallographic structures are therefore reliable. The carbon contents were determined by elemental analysis (< 0.1 wt% for all the samples presented in this manuscript) to exclude any possible contamination.

So, when employing the same gas flow and composition, β-Mo_2N is formed at high ramp (T_{rate} = 5 °C min^{-1}), while a slow ramp (T_{rate} = 0.5 °C min^{-1}) generates γ-Mo_2N. This result agrees with the recent work of Cárdenas-Lizana *et al*. [13] who reported that heating rate is one of the principal parameters determining formation of β-phase (T_{rate} > 2 °C min^{-1}) or γ-phase (T_{rate} ≤ 0.5 °C min^{-1}). Specific surface area (S_{BET}) of β-Mo_2N (16 m^2 g^{-1}) is one of the highest reported for this phase (2-17 m^2 g^{-1}) [13,25,32–34] while the one of γ-Mo_2N (41 m^2 g^{-1}) falls within the range reported in the literature (14-151 m^2 g^{-1}) [13,30]. It is interesting to note that few studies report the nitrogen contents (or Mo/N experimental bulk ratio) and when they do, a wide range of values have been reported for β-Mo_2N_x (5.0 ≤ N (wt%) ≤ 6.6 and 0.72 ≤ x ≤ 0.98) [17,25,36]. It is unclear if this represents a true variation in stoichiometry and degree of nitridation depending on the synthesis condition or if it is due to some differences in experimental data, such as the presence of varying quantities of molybdenum metal between key studies [60]. Regarding the cubic γ phase, a nitrogen content around 6% is usually obtained for syntheses with N_2/H_2 (6.0-6.1%) [17,56] while 9.6% [25] has been reported with NH_3. Due to the incertainty of the analyses, Mo_2N_x is considered completely nitrided for 0.95 ≤ x ≤ 1.00 and 6.5 ≤ N (wt%) ≤ 6.8. Therefore, we report in this study a method allowing the synthesis of tetragonal and cubic molybdenum nitride with full nitridation. For comparisons, a synthesis was conducted with NH_3 where a nitrogen content of 9.5% was obtained (Mo_2N-0.5-NH_3, Table 1, Figure A.2), in agreement with the literature. This excess of nitrogen can be due to NH_x adsorbed on the surface [57] or N present in grain boundaries [18]. TGA analyses under Ar were conducted on these 3 samples (Mo_2N-5, Mo_2N-0.5, Mo_2N-0.5-NH_3). The results (Figure A.4) show that the stability of the nitrogen in these structures follow the order β-Mo_2N > γ-Mo_2N > γ-Mo_2N-NH_3. The sample synthesized under NH_3 release nitrogen (ca. 5 wt%) at low temperature (400 °C) which confirms that the excess of nitrogen is weakly adsorbed.

In an attempt to control the nitrogen content without affecting the crystallographic phase, samples Mo_2N-5-T650 and Mo_2N-0.5-T650 (Table 1, Figure A.2) were synthesized with a final TPN temperature of 650 °C. For T_{rate} = 5 °C min^{-1} pure and fully nitrided β-Mo_2N is still obtained. On the other hand, for T_{rate} = 0.5 °C min^{-1}, the nitridation was not complete and a nitrogen deficit γ-$Mo_2N_{0,91}$ was observed. As expected the lower temperature prevents sintering; molybdenum nitride crystallite

sizes are lower (β-Mo_2N: 13 vs 20 nm; γ-Mo_2N: 7 vs 10 nm) and surface areas are higher (17 and 55 $m^2\ g^{-1}$) in comparison with samples synthesized at 700 °C.

In the literature, it was proposed that the choice of the gas for cooling down (He or N_2) can promote transformation from γ to β-Mo_2N [57,58]. In order to assess this phenomenon, Mo_2N-5-Cool-Ar and Mo_2N-0.5-Cool-Ar were synthesized similarly to Mo_2N-5 (i.e. β-Mo_2N) and Mo_2N-0.5 (i.e. γ-Mo_2N), but Ar was used instead of N_2 in the cooling step (Table 1, Figure A.2). When cooling with Ar (Mo_2N-5-Cool-Ar), β-Mo_2N is formed however some metallic Mo is present. Indeed, desorption of nitrogen takes place under argon at high temperature (0.6 wt% at 700 °C, Figure A.4) during the few hours required for cooling down, as reported elsewhere [57]. It is interesting to note that Mo_2N-0.5-Cool-Ar consists of 5% Mo + 68% β-Mo_2N + 27% γ-Mo_2N, which confirms the transformation of γ to β-phase and the higher stability of the latter one. The simultaneous existence of β and γ-phase at same temperature prove that formation of β and γ-Mo_2N by TPN with N_2/H_2 is a kinetically controlled process [6,34]. From the phase diagram of molybdenum nitride as a function of temperature, pressure and nitrogen concentration, γ-Mo_2N is more stable at higher temperatures, while β-Mo_2N is more stable at lower temperatures [59]. At atmospheric pressure, the transition occurs in the range ca. 480 to 800 °C, with increasing stoichiometry [6,59]. Also, theoretical calculations of enthalpy of formation (ΔE_f) for the two phases revealed that β-phase is slightly more thermodynamically stable than γ (ΔE_f (β)= -1.8836 eV *vs.* ΔE_f(γ)= -1.8049 eV) [49].

It was stated that gas hourly space velocity (GHSV) can impact specific surface area of γ-phase [30,60], while it does not seem to influence the textural structure of β-Mo_2N [13]. In agreement with the literature, a decrease in GHSV for the synthesis of β-Mo_2N (samples Mo_2N-5-GHSV87 and Mo_2N-5-GHSV109, Table 1, Figure A.2) did not impact specific surface area (15-16 $m^2\ g^{-1}$). It is worth noting that the samples were associated with a lower amount of nitrogen (6.4 wt%) corresponding to the formation of $Mo_2N_{0.92}$. The synthesis of pure γ-Mo_2N employing a low GHSV is not possible (Mo_2N-0.5-GHSV87, Table 1, Figure A.2). Indeed, the sample consists of a mixture of 57% β-Mo_2N + 43% γ-Mo_2N revealing that γ-phase is sensitive to the quantity of reactive gas. High space velocities are known to increase the degree of reduction of MoO_3 [61] and facilitate the removal of water from the solid [30,62], reducing hydrothermal sintering. Therefore, the crystallite size of the intermediates might play a crucial role on the crystallographic phase of the nitride.

The reduction/nitridation of MoO_3 was then done with a flow of 85% v/v N_2/H_2 with a temperature program up to 700 °C (Table 1). No matter which T_{rate} was applied we could not obtain unique β or unique γ-phase (Figure A.2). Mo_2N-5-85%N_2 (T_{rate}= 5 °C min^{-1}) sample consists of 27% MoO_2 + 28% Mo + 45% β-Mo_2N indicating that these conditions do not provide complete reduction/nitridation process. This result show that when the hydrogen content is too low, molybdenum oxide is not well

reduced and MoO_2 is still present. Indeed, the temperatures of reduction of the oxides increase with a decrease in H_2 partial pressure or flow rate [30,61]. Mo_2N-0.5-85%N_2 (T_{rate}= 0.5 °C min^{-1}) consists of mixture of β and γ-phase. Therefore, the formation of Mo_2N requires high hydrogen gas space velocity.

Only one study reports the effect of particle size of MoO_3 on the synthesis of γ-Mo_2N [22]. They attributed the increase in surface area of γ-Mo_2N to the easier diffusion of NH_3 in small MoO_3 particles. The influence of MoO_3 particle size was investigated for the first time for β-Mo_2N. After calcination of AHM under air at 350 °C, MoO_3 was sieved and divided in three batches, 40-63 µm, 63-80 µm and 100-315 µm. The BET surface areas, N contents, crystallite sizes and lattice parameters associated with molybdenum nitride are included in Table 2. While for γ-Mo_2N the MoO_3 particle size does not seem to affect the materials (Mo_2N-0.5; Figure A.5 and Table 2), there is a strong effect on β-Mo_2N (Mo_2N-5; Figure A.6 and Table 2). Indeed, a decrease in MoO_3 particle size generates a decrease in the lattice *c* (tetragonal structure) in line with the lower nitrogen content.

Table 2. *Influence of MoO_3 particle size (d_{MoO3}) on the structural properties of Mo_2N.*

Sample name	T_{rate} (°C min^{-1})	d_{MoO3} (µm)	S_{BET} (m^2 g^{-1})	*N (wt%)*[a]	Mo_2N_x *(x)*[a]	d_{Mo2Nx} *(nm)*[b]	*a (Å)*	*c (Å)*
Mo_2N-5-63µ	5	40-63	19	6.2	0.91	23	4.199[c]	8.043[c]
Mo_2N-5-80µ	5	63-80	17	6.3	0.93	20	4.199[c]	8.082[c]
Mo_2N-5-315µ	5	100-315	22	6.7	0.99	21	4.197[c]	8.092[c]
Mo_2N-0.5-63µ	0.5	40-63	40	6.6	0.96	9	4.160[d]	-
Mo_2N-0.5-80µ	0.5	63-80	45	6.6	0.98	9	4.163[d]	-
Mo_2N-0.5-315µ	0.5	100-315	41	6.6	0.97	9	4.163[d]	-

[a] *based on elemental analyses*
[b] *crystallite size based on XRD analyses*
[c] *cell parameters corresponding to tetragonal I41/amd structure (β-Mo_2N)*
[d] *cell parameters corresponding to fcc Pm-3m structure (γ-Mo_2N)*

The SEM pictures associated with MoO_3 show agglomerates of small flake-like particles after calcination at 350 °C (Figure 2a) and platelet-like structure at 700 °C (Figure 2b); the later morphology being similar to the ones reported for commercial MoO_3. Indeed, the morphology of MoO_3 depends primarily on the temperature of calcination of AHM [63]. Tetragonal and cubic molybdenum nitrides were synthesized from these two precursors. In agreement with the literature, β-Mo_2N consists of non-homogeneous small flake-like particles (Figure 2c and Figure A.7a), whatever the morphology of the precursor [32,34].

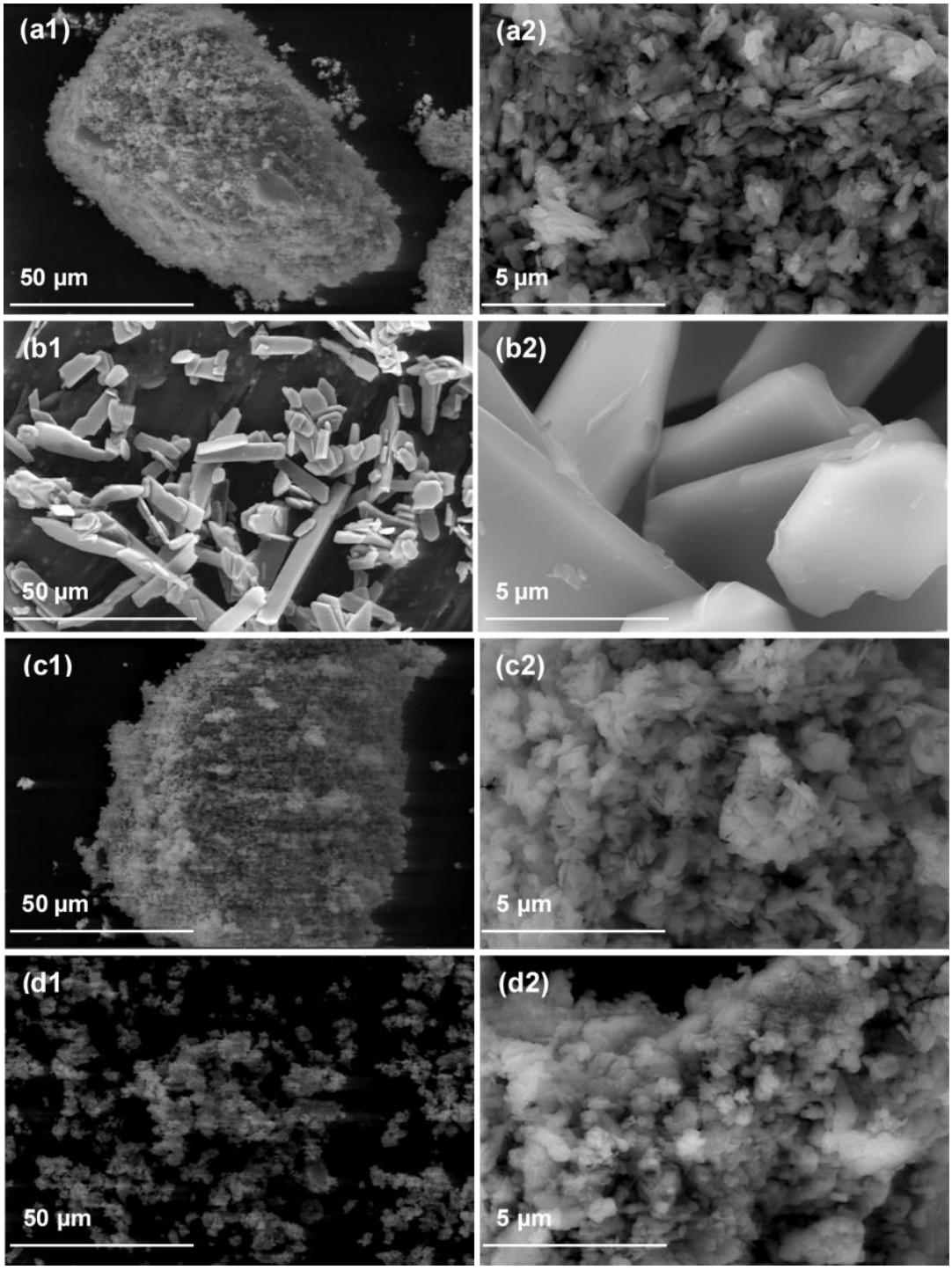

Figure 2. *SEM images of MoO_3 obtained after calcination of AHM at (a1, a2) 350 °C (MoO_3-AHM-350) and (b1, b2) 700 °C (MoO_3-AHM-700); (c1, c2) β-Mo_2N and (d1, d2) γ-Mo_2N obtained from MoO_3-AHM-350.*

In contrary, the morphology of γ-Mo_2N usually correspond to the one of the precursors. Syntheses using commercial MoO_3 [30,62] generates cubic molybdenum nitride with platelet-like morphology while non-homogeneous small particles are obtained from AHM [64]. As revealed by SEM images, γ-

Mo_2N exhibit agglomerates of small flake-like particles in both cases (Figure 2d and Figure A.7b), i.e. we did not observe any changes in morphology. However, the precursor affects the degree of nitridation as the nitrogen contents are lower when starting with MoO_3 calcined at 700 °C (Table 3, Figure A.8). The diffusion and incorporation of nitrogen into the structure might be easier in MoO_3-AHM-350 due to the distinct structural properties. Indeed, the XRD associated with MoO_3-AHM-350 and MoO_3-AHM-700 (Figure A.1c) show orthorhombic structure in the Pnma space group. As expected the sample AHM-700 shows better crystallinity than the MoO_3-AHM-350. The refined crystallite size was found to be 176 ± 50 nm and 34 ± 14 nm, respectively. In addition, the refinement of the crystallite shape shows high anisotropy in agreement with the SEM images.

Table 3. *Effect of temperature of calcination of MoO_3 on the textural properties of Mo_2N.*

Phase	*precursor*	*N (wt%)*[a]	*Mo_2N_x (x)*[a]	*a (Å)*	*c (Å)*	*d_{Mo2Nx} (nm)*[b]	*S_{BET} (m^2 g^{-1})*
β-Mo_2N	MoO_3-AHM-350	6.5	0.96	4.199[c]	8.084[c]	20	15
β-Mo_2N	MoO_3-AHM-700	6.1	0.89	4.198[c]	8.069[c]	21	9
γ-Mo_2N	MoO_3-AHM-350	6.6	0.98	4.164[d]	-	10	41
γ-Mo_2N	MoO_3-AHM-700	6.1	0.90	4.160[d]	-	9	52

[a] *based on elemental analyses*
[b] *crystallite size based on XRD analyses*
[c] *cell parameters corresponding to tetragonal I41/amd structure (β-Mo_2N)*
[d] *cell parameters corresponding to fcc Pm-3m structure (γ-Mo_2N)*

It is worth to mention that previously reported TPN reactions of MoO_3 with N_2/H_2 or NH_3 include multiple steps with different temperature rates and gases [25,33,39,65,66]. We propose here a simple synthesis method by TPN of MoO_3 and 15% v/v N_2/H_2 (GHSV = 230 min^{-1}) at 700 °C, followed by cooling under nitrogen flow. The choice of the temperature rate (0.5 or 5 °C min^{-1}) allow the formation of pure and fully nitrided tetragonal β-Mo_2N or fcc γ-Mo_2N. Moreover, it is possible to tune the degree of nitridation and N vacancies by varying the precursor (the particle size or temperature of calcination), the final temperature or the GHSV.

3.1.2. Formation mechanisms of γ-Mo_2N

As previously reported in section 3.1.1., γ-Mo_2N can be obtained by TPN of MoO_3-AHM-350 under 15% v/v N_2/H_2 gas mixture, at 0.5 °C min^{-1} up to 700 °C, followed by cooling under N_2 and a passivation step. In order to investigate the formation of γ-Mo_2N, other samples were synthesized following the same procedure but reaching the final temperature of 350, 400, 450, 500, 550, 600 and 650 °C. These samples were characterized *ex situ* by XRD (Figure 3), Raman spectroscopy (Figure 4) and elemental analysis (Table 4).

Table 4. *Characterization of the intermediates during the synthesis of γ-Mo_2N.*

Sample name	T_{max} (°C)	*N* (wt%)[a]	*H* (wt%)[a]	*Phases observed by XRD* (wt%)	*Crystallite size associated with each phase (nm)*[b]
	25	< 0.1	< 0.1	MoO_3	MoO_3 (34)
Mo_2N-0.5-T350	350	< 0.1	0.2	62% MoO_3 + 32% MoO_2 + 6% H_xMoO_3	-
Mo_2N-0.5-T400	400	< 0.1	0.2	MoO_2	MoO_2 (33)
Mo_2N-0.5-T450	450	< 0.1	0.1	MoO_2	MoO_2 (64)
Mo_2N-0.5-T500	500	0.5	0.1	MoO_2	MoO_2 (71)
Mo_2N-0.5-T550	550	1.4	-	86% MoO_2 + 14% γ-Mo_2N	MoO_2 (72), γ-Mo_2N (4)
Mo_2N-0.5-T600	600	4.5	-	20% MoO_2 + 3% Mo + 77% γ-Mo_2N	MoO_2 (129), Mo (6), γ-Mo_2N (6)
Mo_2N-0.5-T650	650	6.2	-	γ-Mo_2N	γ-Mo_2N (7)
Mo_2N-0.5-T700	700	6.6	-	γ-Mo_2N	γ-Mo_2N (10)

[a] *based on elemental analyses*
[b] *crystallite size based on XRD analyses*

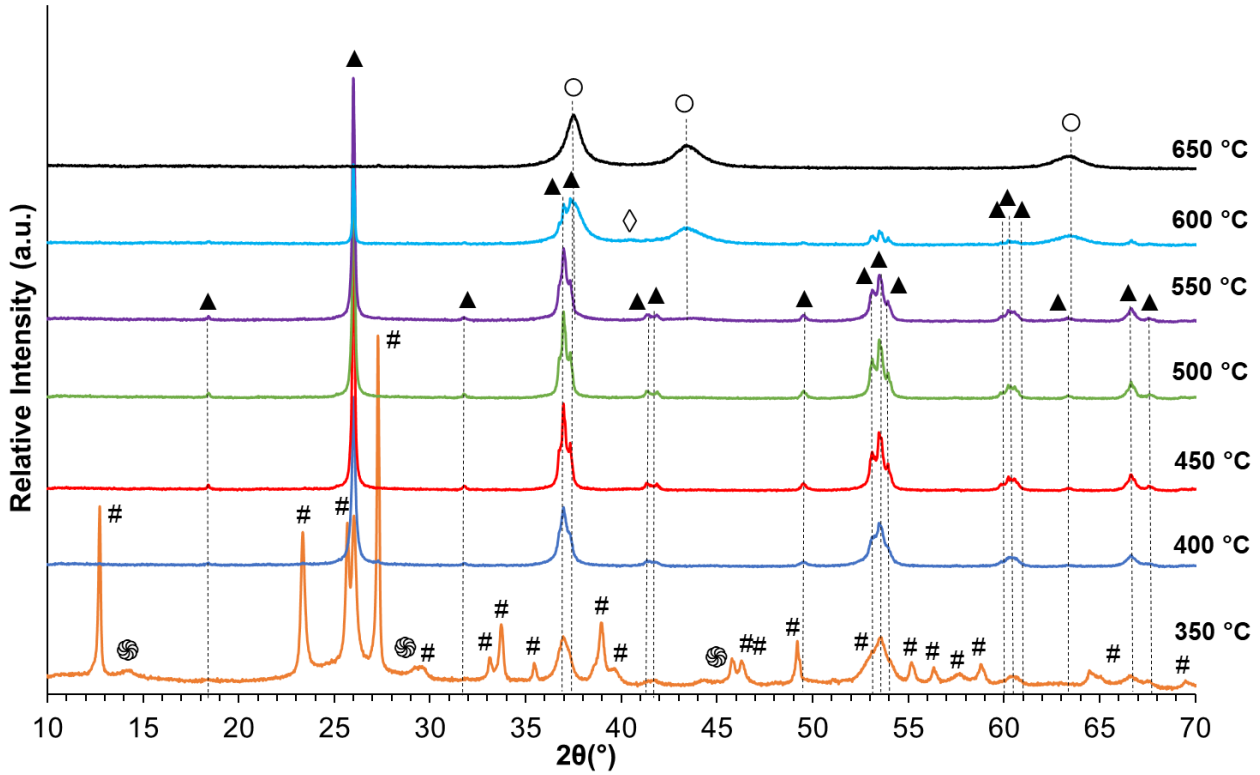

Figure 3. *XRD patterns of Mo_2N-0.5-T350 (350 °C), Mo_2N-0.5-T400 (400 °C), Mo_2N-0.5-T450 (450 °C), Mo_2N-0.5-T500 (500 °C), Mo_2N-0.5-T550 (550 °C), Mo_2N-0.5-T600 (600 °C) and Mo_2N-0,5-T650 (650 °C). Peak assignments based on ICDD files: (#) MoO_3 (PDF 00-035-0609), (▲) MoO_2 (PDF 00-005-0452), (֍) H_xMoO_3, (◊) Mo (PDF 42-1120), and (○) γ-Mo_2N (PDF 00-025-1366).*

As revealed by XRD (Figure 3) the sample at 350 °C consists of a mixture of MoO_3, MoO_2 and an additional phase with peaks at 14°, 29° and 44 °. It is interesting to note that the samples Mo_2N-0.5-T350 and Mo_2N-0.5-T400 contain some hydrogen (0.2 wt%) contrarily to samples treated at higher temperature (Table 4). As the temperature increases, MoO_3 is converted to MoO_2 which was the only phase identified at 450 °C. The main crystallite size of MoO_2 is consistently increasing with temperature, from 33 to 129 nm. Peaks associated with Mo and γ-Mo_2N are observed at 600 °C. According to XRD analysis, the sample synthesized at 650 °C consists of pure γ-Mo_2N. There is no nitrogen below 450 °C, then the nitrogen content increases with the temperature from 0.5 wt% (500 °C) to 6.6 wt% (700 °C, Table 4). It is worth noting that some nitrogen is already in the structure at 500 °C (Table 4) while the XRD diffractogram indicates the only presence of crystalline MoO_2. This suggest the presence of an amorphous nitride or oxynitride phase.

Different mechanisms of formation of γ-Mo_2N from MoO_3 using NH_3 have been proposed in the literature. The transformations usually include MoO_2, Mo and molybdenum oxynitride (MoO_xN_{1-x}) as intermediates. One could think that the additional peaks observed on the XRD diffractogram of Mo_2N-0.5-T350 are connected with an oxynitride phase. However, these XRD peaks do not correlate with XRD patterns of oxynitrides found in JCPDS-ICDD database (PDF 19-8788 and PDF 19-9978) nor with XRD patterns of oxynitrides presented elsewhere [67,68]. Li *et al*. [31] reported an unknown phase with two peaks at 14° and 29 ° that they associated with an oxynitride phase based on the well-accepted mechanism reported [37,64] when using NH_3: $MoO_3 \rightarrow MoO_xN_{1-x} \rightarrow$ γ-Mo_2N. However, Delporte and co-authors [69], who worked on the synthesis of molybdenum carbide, reported X-ray powder diffraction patterns of MoO_3 after H_2 treatment at 350 °C. They observed diffraction peaks at around 14°, 29°, 38° and 44 ° that they attributed to molybdenum oxyhydride with fcc structure. Finally, one study suggests the presence of hydrogen molybdenum bronze (H_xMoO_3) after treatment of MoO_3 with NH_3 at 500 °C, but without evidence [62]. Taking in account that the sample prepared at 350 °C did not contain any nitrogen but 0.2 wt% of hydrogen, the peaks observed at 14, 29 and 44 ° must be related to a molybdenum bronze. To verify this, an additional sample was prepared at 350 °C (0.5 °C min^{-1}) using only H_2 as reductive agent and Ar for cooling (MoO_3-0.5-T350-H_2). As presented in Figure A.9b this sample exhibit a similar diffractogram as Mo_2N-0.5-T350 (Figure A.9a) with the presence of the additional peaks (14, 29 and 44 °) which were attributed to H_xMoO_3 elsewhere [69]. There are five types of bronzes (H_xMoO_3) known and structurally characterized in literature. Neither of these reported structures in the ICSD allowed the indexation of the observed peaks. The qualitative analysis of the collected PXRD data showed a possible indexation of the bronze structure in the Fd-3m space group of the cubic system, in the pyrochlore $Cs_xMo_2O_6$ structure type [70,71]. The observed

additional peaks were successfully refined in the latter structure type with a = 10.632 Å, V = 1201.8 $Å^3$.

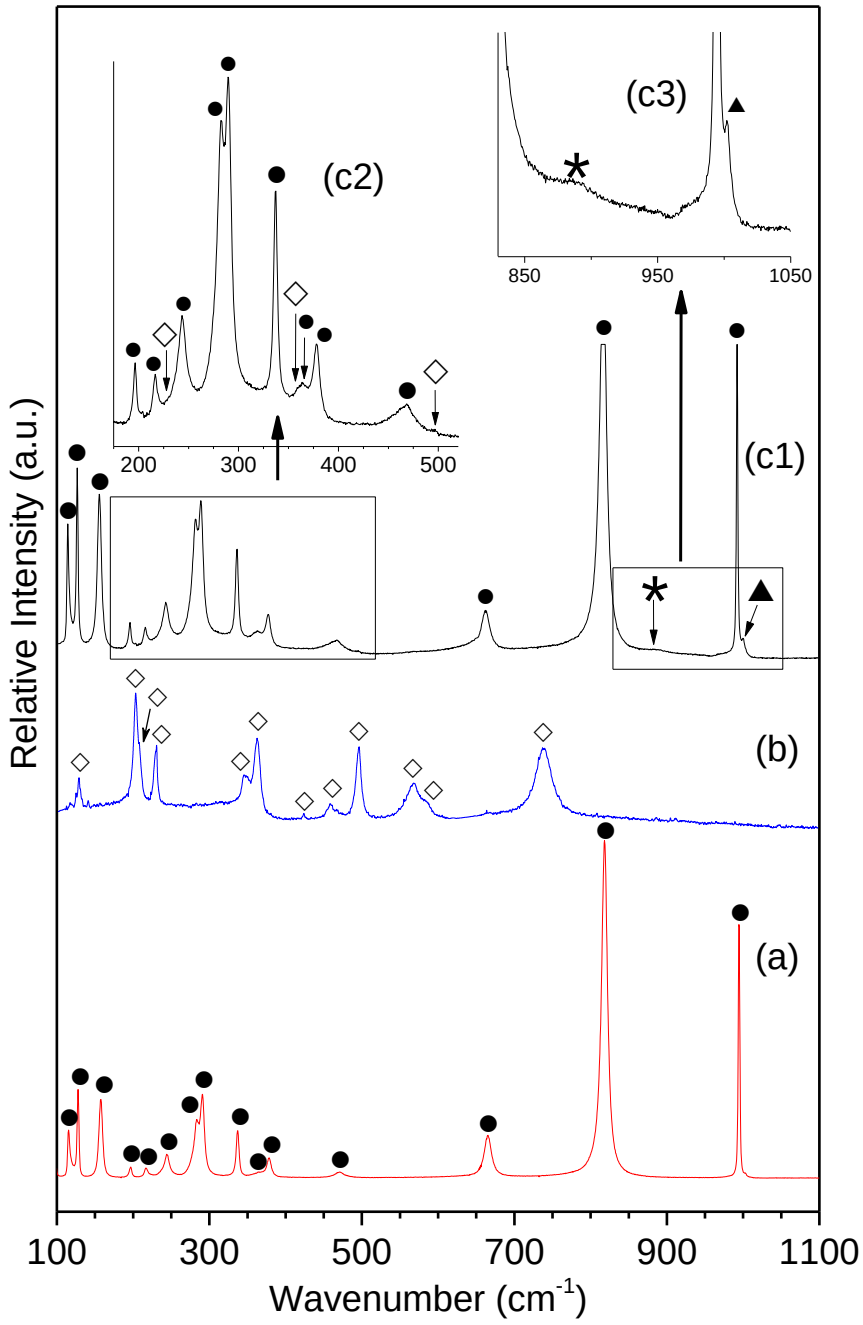

Figure 4. *Raman spectra of (a) MoO_3-AHM-350 (MoO_3), (b) Mo_2N-0.5-T550 (MoO_2) and (c) Mo_2N-0.5-T350; with attributed bands, MoO_3 (●), MoO_2 (◊), Mo_5O_{14} (*), H_xMoO_3 (▲).*

Figure 4 shows Raman spectra of MoO_3-AHM-350, Mo_2N-0.5-T350 and Mo_2N-0.5-T550. In Figure 4a, the bands at 116, 128, 158, 197, 217, 244, 283, 291, 338, 364, 378, 471, 666, 819 and 995 cm^{-1}, coincide with previously reported data for orthorhombic MoO_3 [72,73]. Sample Mo_2N-0.5-T550

(Figure 4b) presents characteristic Raman shifts of MoO_2 at 127, 201, 206, 229, 344, 361, 423, 457, 496, 567, 582 and 738 cm^{-1} [74]. The small amount of Mo and Mo_2N in Mo_2N-0.5-T550 (Table 4) do not contribute to the spectrum as there are not active for Raman analysis. Considering the sample Mo_2N-0.5-T350 (Figure 4c1, 4c2, 4c3), the bands associated mainly with MoO_3 and in small proportion with MoO_2, were present, and some additional bands were observed at 893 and 1003 cm^{-1}. The small band at 893 cm^{-1} might be due to a Mo_5O_{14} type oxide [75]. It was reported in the literature [72] that Raman spectrum of type I bronze ($H_{0,30}MoO_3$) is very similar to that of MoO_3 with some additional bands at 452, 670, 750 and 1011 cm^{-1}. This is consistent with our spectrum, as a band at 1003 cm^{-1} is clearly visible while the other three bands overlap with bands associated with MoO_3 and MoO_2. Ou *et al.* [76] also attributed a band at 1005 cm^{-1} to molybdenum bronze. Finally, the Raman spectra of MoO_3-0.5-T350-H_2 (Figure A.10) is similar to the one of Mo_2N-0.5-T350.

Based on our results, we can propose for the first time a mechanism for the formation of γ-Mo_2N employing a mixture of N_2/H_2: $MoO_3 \rightarrow H_xMoO_3 \rightarrow MoO_2 \rightarrow Mo \rightarrow$ γ-Mo_2N.

3.1.3. Formation mechanisms of β-Mo_2N

Table 5. *Characterization by XRD of the intermediates during in-situ synthesis of β-Mo_2N.*

Sample name	*$T_{analysis}$ (°C)*	*Phases observed (wt%)*	*Crystallite size associated with each phase (nm)*
Mo_2N-5-25	25	MoO_3	-
Mo_2N-5-350	350	75% MoO_3 + 21% MoO_2 + 4% H_xMoO_3	-
Mo_2N-5-400	400	41% MoO_3 + 59% MoO_2	MoO_3 (47), MoO_2 (36)
Mo_2N-5-450	450	3% MoO_3 + 97% MoO_2	MoO_3 (44), MoO_2 (43)
Mo_2N-5-500	500	98% MoO_2 + 2% β-Mo_2N	MoO_2 (44), β-Mo_2N (11)
Mo_2N-5-550	550	91% MoO_2 + 6% Mo + 3% β-Mo_2N	MoO_2 (47), Mo (6), β-Mo_2N (7)
Mo_2N-5-600	600	52% MoO_2 + 31% Mo + 17% β-Mo_2N	MoO_2 (57), Mo (9), β-Mo_2N (4)
Mo_2N-5-650	650	9% MoO_2 + 70% Mo + 21% β-Mo_2N	MoO_2 (55), Mo (17), β-Mo_2N (6)
Mo_2N-5-700	700 + ¼ h	75% Mo + 25% β-Mo_2N	Mo (30), β-Mo_2N (8)
Mo_2N-5-700b	700 + 3 h	15% Mo + 85% β-Mo_2N	Mo (20), β-Mo_2N (19)
Mo_2N-5-700c	700 + 6 h	4% Mo + 96% β-Mo_2N	Mo (14), β-Mo_2N (21)

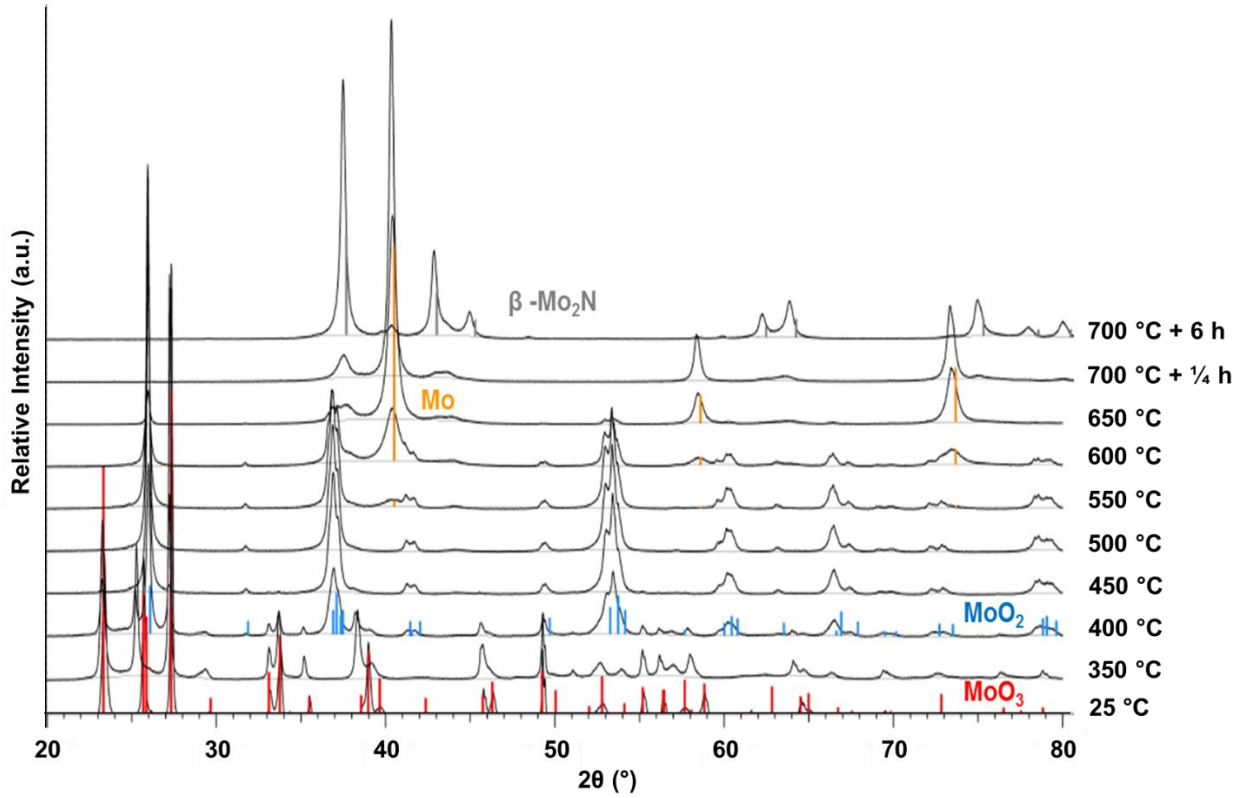

***Figure 5**. In situ XRD performed until 700 °C (T_{rate} = 5 °C min^{-1}) under 15% v/v N_2/H_2 (35 mL min^{-1}, GHSV=109 mL min^{-1}).*

As previously reported in section 3.1.1., β-Mo_2N can be obtained when using a temperature ramp of 5 °C min^{-1}. This rapid ramp can be used with the heating chamber for XRD allowing to monitor *in situ* the formation mechanism of β-Mo_2N. Experiment was conducted under 15% v/v N_2/H_2 flow until 700 °C (T_{rate} = 5 °C min^{-1}) and diffractograms were recorded every 50 °C in the temperature range of 350-700 °C (Table 5, Figure 5). The results indicate that intermediates in the formation mechanism of β-Mo_2N include MoO_2 and Mo metallic, as previously reported in the literature [31,33–35]. However, there is still some metallic Mo present at 700 °C, which is converted to β-Mo_2N with time (only 4% of Mo left after 6 h). It is possible to obtaine pure β-Mo_2N by running the experiment over a longer time (12 h at 700 °C). This is in different from the sample Mo_2N-5-GHSV109 (Table 1) where only pure β-Mo_2N was obtained using an identical GHSV of 109 min^{-1}. The main differences between these two syntheses rely on the design of the reactor: in the XRD chamber ca. 0.3 g of powder was placed under a flow (35 mL min^{-1}) through a licked bed, i.e. swept on the surface, while in the reduction/nitridation cell ca. 2 g of powder was placed in a flow (253 mL min^{-1}) through a cross-bed vertical quartz cell. These results show that the configuration of the reactor can affect the formation of the molybdenum nitride due to differences in diffusion of the gases into the material.

Additionally, at 350 and 400 °C, a broad peak can be observed at around 29°. Despite the quality of the data, the additional peaks could be associated with a new H_xMoO_3 bronze structure crystallizing in the pyrochlore $CsMo_2O_6$ structure type. To clarify this, Mo_2N-5-T350 and MoO_3-5-T350-H_2 were synthesized in the reduction/nitridation cell at 350 °C with either a flow of N_2/H_2 or H_2. Elemental analysis for both samples confirmed the absence of nitrogen and the presence of hydrogen (0.2 wt%). As shown by XRD (Figure A.9) and Raman (Figure A.10) analyses, these two samples are similar to Mo_2N-0.5-T350 and MoO_3-0.5-T350-H_2 and consist of MoO_3, MoO_2 and H_xMoO_3. The phase quantification (wt%) by the Rietveld method led to the presence of MoO_3 (75%), MoO_2 (21%), $HxMoO_3$ (4%). Therefore, we can propose a new mechanism for the formation of β-Mo_2N: MoO_3 → H_xMoO_3 → MoO_2 → Mo → β-Mo_2N.

3.1.4. Monitoring the nitridation process of β-Mo_2N using *in situ* XPS and UPS

Understanding the elementary steps occurring during the synthesis of β-Mo_2N is a fundamental challenge to determine its active phase. While air exposure after passivation does not impact the bulk structure (assessed by Raman spectroscopy and X-Ray diffraction analysis), it has a strong impact on the degree of oxidation of the metal species at the surface. In this context, the identification of the chemical state and electronic structure of Mo_2N requires an in-depth characterization under *in situ* conditions. For the first time, X-ray/UV Photoelectron Spectroscopy (XPS/UPS) were conducted during each stage of the synthesis, passing through the oxidation of heptamolybdate precursor and its subsequent nitriding phase, all carried out under relevant synthesis conditions.

In situ preparation of the sample was carried out using an atomic liquid injection system (ALI) connected to the vacuum XPS/UPS setup. A solution of AHM ($(NH_4)_6Mo_7O_{24}\cdot 4H_2O$) was injected at high pressure under vacuum conditions ($<10^{-6}$ Torr) on a piece of Ag foil previously prepared. Subsequently, the chemical states at the surface of the coating were followed by XPS (Figure 6), highlighting the presence of Mo 3d, Mo 3p, and N 1s core levels. In particular, N 1s exhibit NH groups [77] at ≈ 401 eV corresponding to NH in AHM precursor. Mo^{6+} state and reminiscent Mo^{5+} are present in Mo 3p and Mo 3d core levels (Figure 6(i)). Mo^{6+} and NH chemical states confirmed the injection and growing of AHM onto the Ag support. The presence of Mo^{5+} is attributable to X-ray photoreduction [78]. Then, the AHM coating was oxidized under O_2 flow during 2 h at 250 °C *in situ* in order to decompose and transform the precursor into MoO_3. This transformation is confirmed by Mo 3p, N 1s, and Mo 3d core levels (Figure 6(ii) through the disappearance of NH state. The formation of MoO_3 was confirmed by UPS (Figure 7a), which exhibits a large band mainly constituted by O 2p orbitals center at ≈ 6.9 eV with a bandwidth between 6 and 8 eV associated with MoO_3 [79]. This UPS

analysis allows to discard the presence of MoO_2 after *in situ* oxidation, as this spectrum does not reveal *intra*-gap states, which are usually located between 0 eV and 2 eV [79].

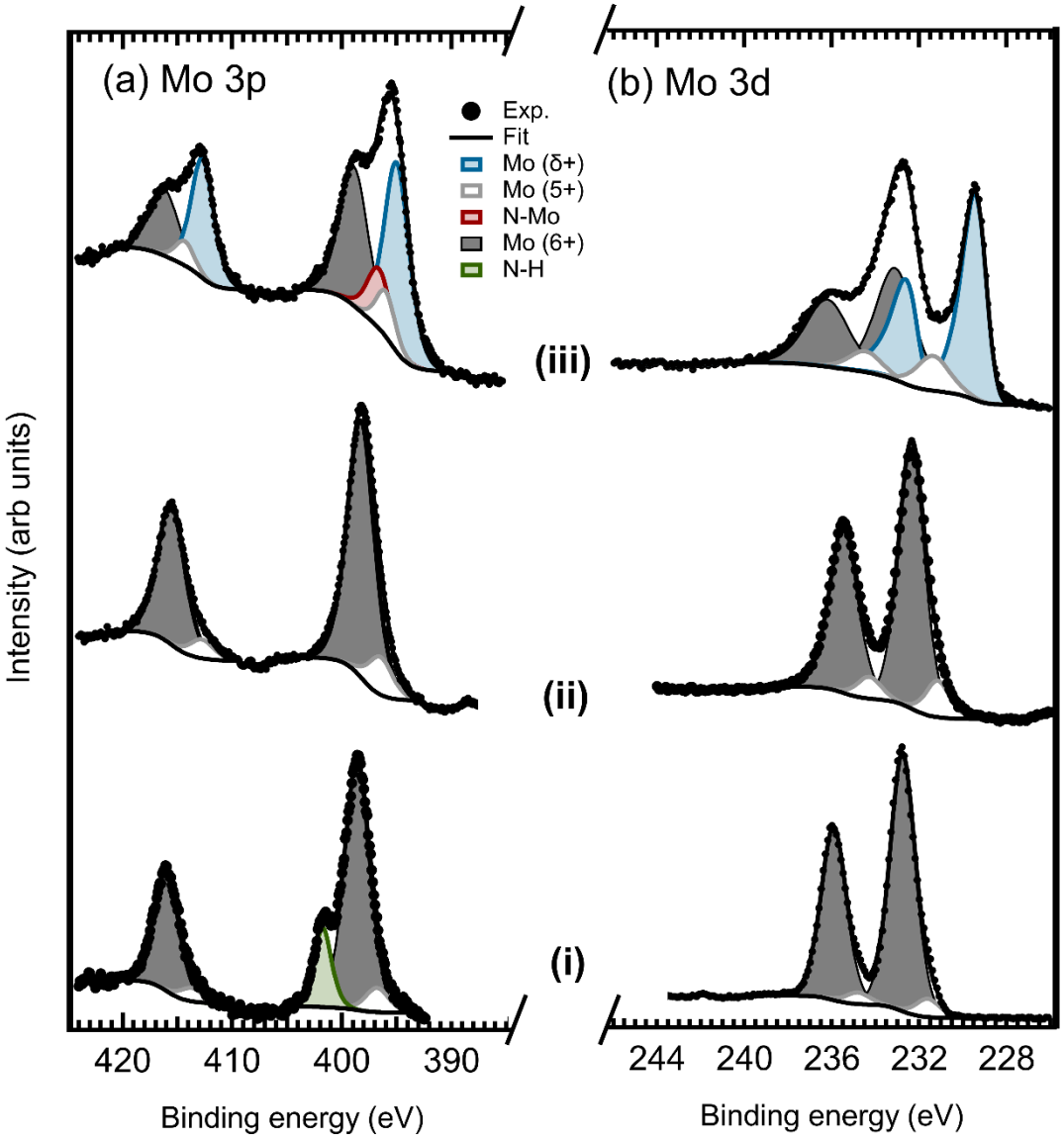

Figure 6. *(a) Mo 3p, N 1s and (b) Mo 3d core levels (XPS) of AHM (i) coated on Ag foil, (ii) after in situ oxidative treatment and (iii) after TPN under 15% v/v N_2/H_2 flow at 5 °C min^{-1} up to 700 °C.*

Afterward, the nitridation was carried out under 15% v/v N_2/H_2 flow (40 mL min^{-1}) at 5 °C min^{-1} up to 700 °C and hold for 3 h. This treatment was executed under *in situ* conditions without exposing the sample to air. Those conditions are analogous to the ones that yielded to β-Mo_2N (Mo_2N-5), but they differ in term of reactor and GHSV. In Figure 6(a)-(iii), the Mo 3p core level reveals seven components containing six Mo $3p_{3/2}$ - Mo $3p_{1/2}$ spin-orbit split doubles and one contribution corresponding to the N 1s core level. The fit results of Mo 3d (Figure 6(b)) and Mo 3p (Figure 6(a)) corroborate each other.

The presence of N and $Mo^{\delta+}$ state confirmed the formation of Mo nitride [38]. Mo ($3d_{5/2}$ δ+) in Mo 3d core level appears at 229.4 eV; this position should not be confused with 230 eV associated with Mo ($3d_{5/2}$ 4+) and is located higher than Mo ($3d_{5/2}$ 0) at 227.8 eV. Therefore, Mo (δ+) is attributable to an intermediate state between 0 < δ < 4. The presence of this *quasi*-metallic state is confirmed by the *intra*-gap states visible in the valence band between 0 and 2 eV (Figure 7(a)). Both spectral features highlight a strong metallic character [49].

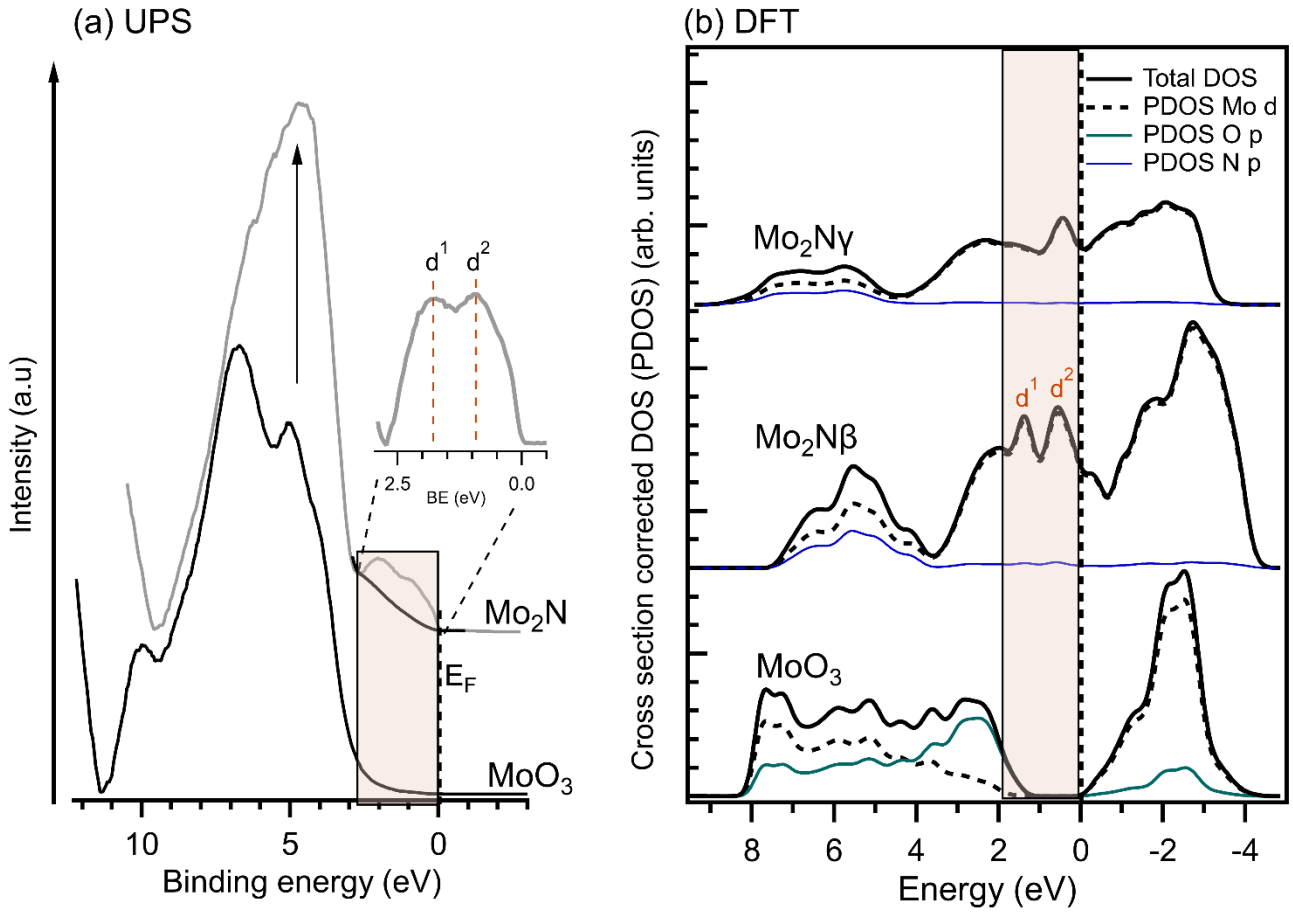

Figure 7. *(a) Valence band (UPS) of AHM after oxidative treatment (bottom, MoO_3), and subsequent nitridation/reduction treatement (Top: Mo_2N). Insert: zoom of the 0 – 2.5eV region with subtraction of the Li background [41], (b) Projected density of states (PDOS) calculated using DFT for MoO_3 (bottom), $Mo_2N\beta$ (middle) and $Mo_2N\gamma$ (top). All PDOS were normalized by PICS [53].*

Although theoretical studies have been used to predict the electronic structure of molybdenum nitrides [49,50,80], none of these were corroborated by an experimental analysis of the valence band by UPS. The UPS spectra were analyzed following an analytical procedure developed to precisely determine quantitative parameters, such as position and relative intensity [42]. Figure 7(a) shows a clear spectral evolution during the nitridation/reduction treatment. First, the O 2p region is substantially modified with a strong component located at 4.6 eV (see arrow-Figure 7(a)), which could be related to N 2p state from DFT calculations. Second, *intra*-gap states appear, with two bands at 0.85

eV (d^2) and 1.65 eV (d^1) [79]. The projected density of states (PDOS) of MoO_3, γ-Mo_2N and β-Mo_2N were computed using DFT and then normalized by photo-ionization cross-sections (PICS) (see experimental details) and shown in Figure 7b. Two peaks are clearly visible below the Fermi level of β-Mo_2N while only one peak appears in the case of γMo_2N. Furthermore, for β-Mo_2N the relative splitting energy between the two peaks is 0.84 eV, which coincides with the experimentally observed value. This confirms that here also using a temperature ramp of 5°C min^{-1}, the β-Mo_2N phase is obtained during this *in situ* synthesis.

3.1.5. Discussion related to the mechanisms: β-Mo_2N vs γ-Mo_2N

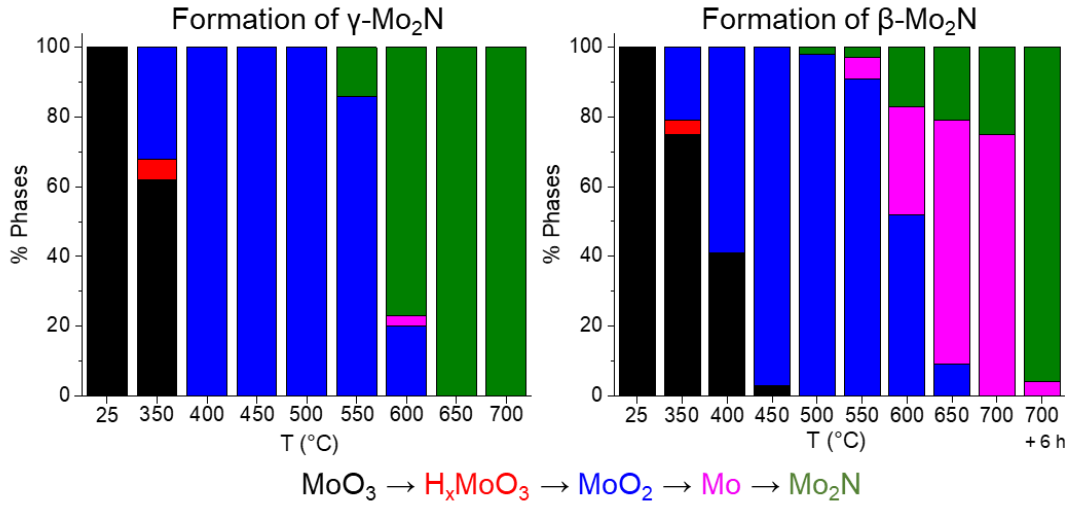

Figure 8. *Percentage of the different crystallographic phases in the samples as a function of temperature: MoO_3 (black), H_xMoO_3 (red), MoO_2 (blue), Mo (magenta) and molybdenum nitride (green). Results based on Table 4 (γ-Mo_2N: T_{rate} = 0.5 °C min^{-1}, GHSV=230 mL min^{-1}) and Table 5 (β-Mo_2N: T_{rate} = 5 °C min^{-1}, GHSV=109 mL min^{-1}).*

Surprisingly, the intermediates for the tetragonal and cubic structures are the same and the mechanisms go through the same route. The temperature rate and GHSV are the key parameters affecting the crystallographic phase. The low temperature rate but more importantly the high GHSV necessary for the formation of γ-Mo_2N prevented us to conduct its synthesis *in situ*. Different attempts were made with the XRD chamber employing slow heating rate (≤ 1 °C min^{-1}) but GHSV no higher than 109 h^{-1} could be used. A mixture of β-Mo_2N and γ-Mo_2N was then obtained, in agreement with results obtained in Table 1. During the synthesis of γ-Mo_2N (Figure 8), metallic Mo is hardly present as it is quickly transformed to the nitride. Hence, the rate of reduction and nitridation are similar and the phenomena occur simultaneously, in the same range of temperature. The crystallite size of Mo and γ-Mo_2N remain low (< 10 nm, Table 4). In contrary, when higher rate (5 °C min^{-1}) and lower GSHV

are used, the reduction of MoO_2 to Mo occurs first, it is then followed by nitridation to β-phase. The rate of nitridation is slower than the reduction. Therefore, the crystallite sizes of Mo increase with temperature up to 30 nm, before nitridation (Table 5). Formation of water during the reduction causes hydrothermal sintering [30,62]. The slow heating and high GHSV facilitate the removal of water from the solid and prevent sintering of the intermediates while high content of water inhibits the nitridation. Moreover, the larger the particles, the slower the diffusion of N_2 into the Mo structure. It has been reported that the particle size is a crucial parameter on determining molybdenum and tungsten carbides phase [81]. The cubic phases are predominant at small particle sizes while the hexagonal phases are favored at larger sizes. Our results suggest that the same phenomena occur with molybdenum nitride and the crystallite size of Mo plays a crucial role on the final crystallographic phase. Small and large crystallite of Mo favor the formation of γ- and β-phase, respectively. In addition, it seems that crystallites of γ-Mo_2N are stable at small size (5-10 nm) while β-Mo_2N growths quickly to larger particles (19-21 nm). In order to investigate this theory, additional experiments were conducted. First, Mo metallic was synthesized by heating MoO_3 under H_2 flow to 700 °C, applying different T_{rate} (5 and 0.5 °C min^{-1}). In both cases pure Mo was obtained with large crystallite sizes (80 and 119 nm, Table A.1). Then TPN with N_2/H_2 flow (standard conditions, as for Mo_2N-5 and Mo_2N-0.5) of these two Mo samples was done and, in both cases, only β-Mo_2N was obtained (Table A.1). This result shows that it is not possible to form γ-phase from large Mo particles. Additionally, large particles inhibit the nitridation as some Mo metal is still present at the end of the syntheses. We can conclude that the formation mechanisms of β and γ-phase include the same intermediates (molybdenum bronze-H_xMoO_3, MoO_2 and Mo). The heating rate (T_{rate}) and GHSV affect the removal of the water and the diffusion of gases into the structure, and the crystallite sizes, notably of Mo (Scheme 1). These parameters affect the thermodynamic and kinetics of the reduction and nitridation, hence the final crystallographic phase.

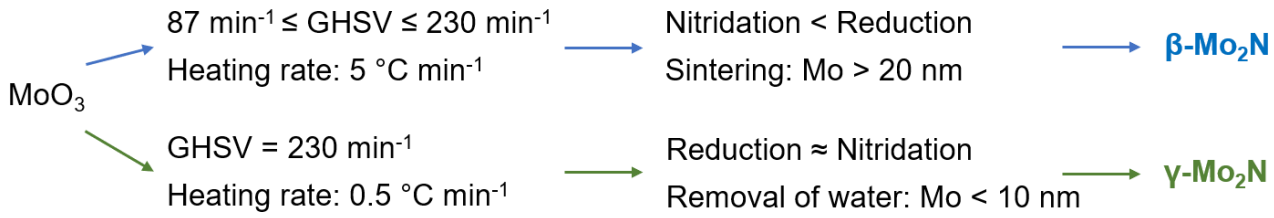

Scheme 1. *Main parameters affecting the final crystallograhic phase of molybdenum nitride.*

3.2. Molybdenum nitride supported on TiO_2 and CeO_2

Regarding supported molybdenum nitride, there is significantly less information on the effect of the preparation method on their structure. They are usually prepared by standard impregnation of the support with an aqueous solution of Mo precursor, followed by calcination and reduction/nitridation

steps at 700 °C (TPN with NH_3 or N_2/H_2). The support can influence the completion of reduction/nitridation process, the nitride dispersion, the crystallographic phase and the nitrogen content [18,19,26,66,82]. A study focused on 12% Mo_2N-supported on alumina, silica, zirconia and titania synthesized by TPN of MoS_2 with NH_3 [83]. The results showed that the crystallite size of the nitride phase (10-20 nm) depended on the nature support, but it was independent of the surface area of the support as the best dispersion was obtained on ZrO_2. More recently, another group [82] studied the influence of the supports (Al_2O_3, TiO_2, ZrO_2, silicas and zeolites) on the crystallographic phase obtained by TPN of a complex of ammonium heptamolybdate and hexamethylenetetramine with 20% v/v N_2/H_2. They observed the formation of β-Mo_2N on Al_2O_3, the presence of both β- and γ-phase on TiO_2 and ZrO_2, while Mo_3N_2 and Mo_3N_4 were also formed on the more acidic SBA-15 and BEA. Similarly to the bulk material, the source of nitrogen can affect the crystallographic phase where NH_3 and N_2/H_2 promoted the formation of γ-Mo_2N/SBA-15 and β-Mo_2N/SBA-15, respectively [18]. Finally, during the synthesis of γ-Mo_2N/Al_2O_3 by TPN with NH_3, it was reported that an increase in temperature rate and in molybdenum content generated an increase in nitride crystallite size [19]. We could not find any methodological study on the synthesis of molybdenum nitride by impregnation of TiO_2 and CeO_2 with an aqueous solution of ammonium molybdate tetrahydrate followed by TPN with N_2/H_2.

3.2.1. Impregnation and calcination

AHM/TiO_2 and AHM/CeO_2 were prepared by wet impregnation of the support with an aqueous solution of AHM (nominal Mo loading: 9.8 wt%). After drying, these materials were calcined in air at 350 °C, and labeled MoO_3/TiO_2 and MoO_3/CeO_2. The TGA analyses under air of AHM, AHM/TiO_2 and AHM/CeO_2 are presented in Figure A.11. The successive mass losses during the decomposition of AHM are consistent with the literature [63] and attributed to the weakly bonded and structurally intercalated crystalline water molecules and ammonium ions. The transformation of AHM occurs at lower temperature (below 320 °C) for the supported materials, with a weight loss (ca. 2.6 wt%) consistent with the Mo loading. ICP analyses revealed an exact Mo content of 9.4 wt% on TiO_2, equivalent to 14 $atom_{Mo}\ nm^{-2}$, which corresponds to roughly 3 monolayers. Nitrides supported on CeO_2 exhibit 6 $atom_{Mo}\ nm^{-2}$ (9.0 wt%) which is close to the monolayer.

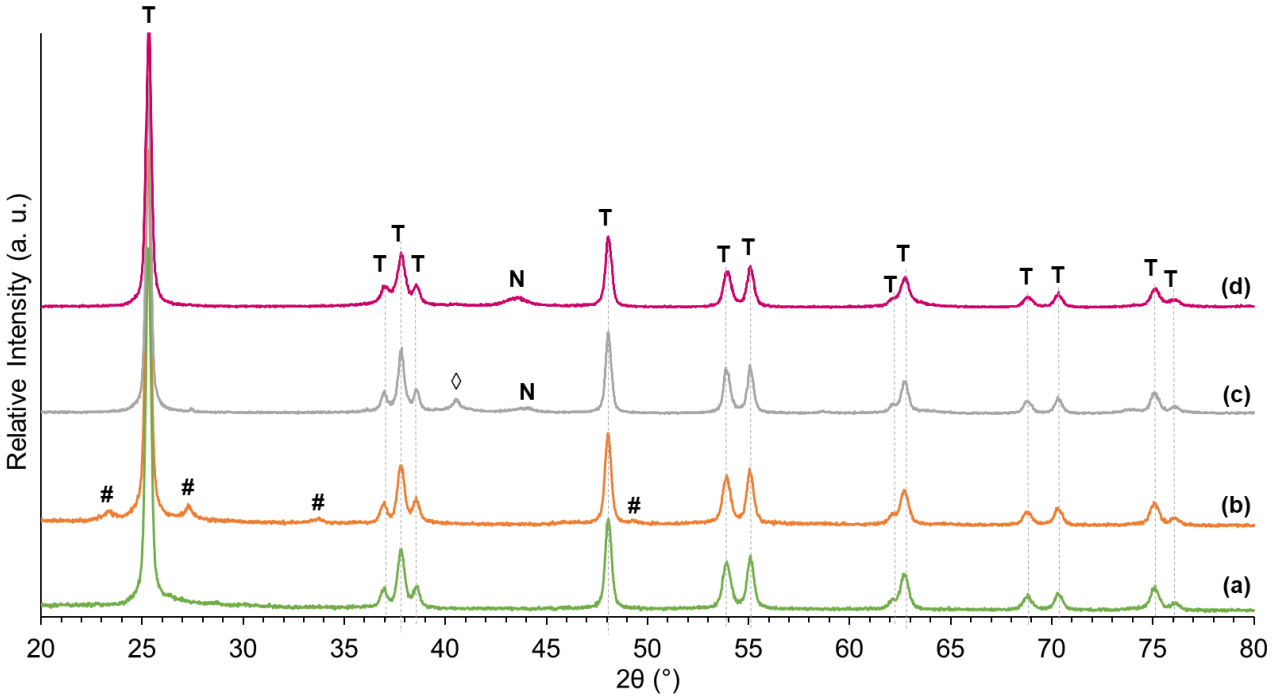

Figure 9. *XRD patterns associated with nitride supported on TiO_2: (a) AHM/TiO_2, (b) MoO_3/TiO_2, (c) Mo_2N/TiO_2 (5-T700-2), (d) Mo_2N/TiO_2 (0.5-T700-2). Peak assignments based on ICDD files: (#) MoO_3 (PDF 00-035-0609), (◊) Mo (PDF 42-1120), (**T**) TiO_2 anatase (PDF 00-021-1272), (**N**) Mo_2N (β-Mo_2N: PDF 01-075-1150 and γ-Mo_2N: PDF 00-025-1366).*

The XRD diffractogram (Figure 9) of AHM/TiO_2 and MoO_3/TiO_2 show the characteristic peaks of TiO_2 anatase phase. The sample after calcination also presents the main peaks of crystalline orthorhombic MoO_3. Raman spectroscopy confirmed the results obtained by XRD for these two samples (Figure 10a). Indeed, Raman spectrum for AHM/TiO_2 consists of characteristic TiO_2 Raman shifts [84] at 143, 195, 397, 516 and 638 cm^{-1}, and a band at 955 cm^{-1} associated with AHM [85]. This later band disappear after calcination and new bands at 285, 335, 815 and 995 cm^{-1} attributed to orthorhombic MoO_3 appear [72,86]. Considering AHM/CeO_2 and MoO_3/CeO_2, we could not detect the presence of crystalline MoO_3 by XRD (Figure A.12) since Mo surface loading is close to Mo-monolayer (6 $atom_{Mo}$ nm^{-2}). Nevertheless, the presence of Mo species was confirmed by Raman spectroscopy (Figure 10b). Raman spectrum of AHM/CeO_2 consists of characteristic dominant bands at around 462 cm^{-1} typical of CeO_2 [86,87] and bands associated with amorphous AHM [85]. For MoO_3/CeO_2, we can observe that the bands associated with AHM are still present along with nanocrystalline MoO_3 (825 and 980 cm^{-1}) [88].

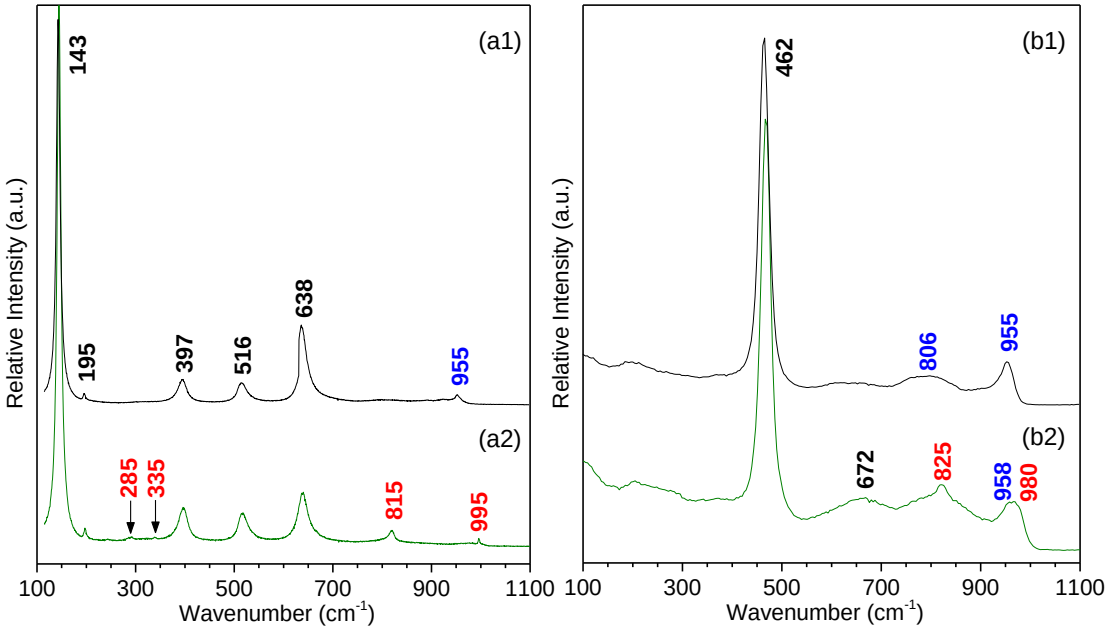

Figure 10. *Raman spectra associated with (a1) AHM/TiO_2, (a2) MoO_3/TiO_2. (b1) AHM/CeO_2 and (b2) MoO_3/CeO_2. Bands associated with the supports (black), AHM (blue), MoO_3 (red).*

3.2.2. Reduction/nitridation

The profiles of the TGA analysis under 3% v/v H_2/Ar flow coupled to MS analysis of the bulk MoO_3, TiO_2, CeO_2, MoO_3/TiO_2 and MoO_3/CeO_2 are presented in Figure A.13. The mass spectrum of the evolved gas was recorded and the only signals observed were at m/z = 17 and 18, which correspond to the formation of water caused by reduction. The reduction of MoO_3 starts at 500 °C during the TGA analysis. This temperature is higher than what we observed during the synthesis of bulk nitrides, which is due to a kinetic effect (different apparatuses and GHSV). The reduction profile associated with MoO_3/TiO_2 presents a mean peak around 470 °C which is consistent with the literature, where values in the range of 491 to 558 °C have been reported for MoO_3/TiO_2 depending on Mo loading [89]. The profile associated with CeO_2 does not present any mass loss beside the one around 100 °C which can be ascribed to the moisture desorption. The reduction of bulk CeO_2 typically occur around 830-850 °C [90]. A second peak can be present at lower temperature (500-550 °C) for CeO_2 with high surface area due to the reduction of surface Ce^{4+}. The reduction of MoO_3 on CeO_2 occurs over a larger range of temperature than MoO_3/TiO_2 and seems to be the combination of two reduction phenomena (392 and 535 °C). The temperature of reduction depends on the oxide-support interaction which is linked to the structure, morphology and crystallite size of the oxide. It has been reported for MoO_3/CeO_2 that the first peak is associated with the reduction of surface Ce^{4+} or octahedral Mo^{6+}, while the peak at higher temperature corresponds to the reduction of crystalline MoO_3 [90].

It is interesting to note that the synthesis of supported nitride is usually conducted at 700 °C. Only one research group studied the impact of the final nitridation temperature during the synthesis of Mo_2N/Al_2O_3 by TPN with NH_3. The results [16] showed that MoO_2 is present at 500 °C, γ-Mo_2N is formed at 700 °C and converted to Mo at 900 °C. However, the thermogravimetric analyses under H_2 showed that the reduction of MoO_3 starts at lower temperatures for supported samples than for the bulk, which might also impact the temperature of nitridation. Therefore, the effect of the final temperature of reduction/nitridation was studied first on TiO_2, and then on CeO_2.

The supported molybdenum nitrides were synthesized by first applying the same procedure as for the bulk materials starting with MoO_3/TiO_2: the temperature was increase at 5 or 0.5 °C min^{-1} up to 700 °C and hold for 2 h (samples are labeled 5-T700-2 and 0.5-T700-2, respectively). The identification of molybdenum nitrides on the supports by XRD was more challenging since (i) the peaks of nitrides and supports can overlap, (ii) the nitride peak intensities are now lower due to low amount of molybdenum, and (iii) the nitride phases might be well dispersed. The main properties (XRD, S_{BET}, N wt%) obtained for Mo_2N/TiO_2 are presented in Table 6 and Table A.2.

Table 6. *Influence of heating rate (T_{rate}), temperature maximal (T_{max}) and time of hold (iso) on Mo_2N/TiO_2 structural properties*.

Mo_2N/TiO_2 Synthesis condition[a]: T_{rate}-T_{max}-iso	Composition and crystallite size (nm)[b]	S_{BET} (m^2 g^{-1})	N (wt%)[c]	Mo_2N_x (x)[c]
5-T700-2	Mo (11), Mo_2N (5)	34	-	-
5-T700-24	Mo (15), Mo_2N (6)	-	-	-
5-T500-2	Mo_2N (9)	-	0.14	0.21
5-T500-24	Mo_2N (5)	49	0.65	0.96
0.5-T700-2	Mo_2N (5)	27	1.18	1.73
0.5-T500-24	Mo_2N (6)	46	0.65	0.96

[a] *gas composition: 15% v/v N_2/H_2*
[b] *composition and crystallite size based on XRD analyses*
[c] *based on elemental analyses*

The XRD diffractograms associated with Mo_2N/TiO_2 (5-T700-2) and Mo_2N/TiO_2 (0.5-T700-2) are included in Figure 9. The main peak associated with Mo_2N phase at ca. 37° is hidden by dominant peaks of TiO_2 between 36° and 39°. Another peak is visible at 44° but it does not allow to determine with certainty the nitride crystallographic phase, even if Rietveld refinement suggest the presence of the tetragonal phase for Mo_2N/TiO_2 (5-T700-2) and the cubic phase for Mo_2N/TiO_2 (0.5-T700-2). These would agree with the results obtained for the bulk nitrides. The co-presence of metallic Mo (main peak at 40.5°) reveals that we did not reach full nitridation when employing a fast heating rate (sample Mo_2N/TiO_2 5-T700-2). The chemical analysis of Mo_2N/TiO_2 (0.5-T700-2) gave a nitrogen content of 1.18 wt% and Mo content of 9.9 wt%, which corresponds to $Mo_2N_{1,73}$ stoichiometry. (N/Mo ratio much higher than for Mo_2N). The TiO_2 lattice parameters remain the same before and after reduction/nitridation (Table A.2) and TiN was not observed by XRD. Therefore the excess of N-atoms are adsorbed on the support surface as NH_x but not incorporated into the structure of the support [18,26,39]. It is worth mentioning that the presence of Mo species prevent the transformation of anatase to rutile which usually occur between 600 °C and 700 °C [91], as previously reported [92]. Despite the calcination of the support at 700 °C under air before impregnation, the reduction/nitridation step generated a slight decrease in specific surface area, from 48 to 27 and 34 $m^2\ g^{-1}$ (Table 6). To conclude on the reduction/nitridation at 700 °C, for T_{rate} = 5 °C min^{-1} the nitridation is not complete while in the case of T_{rate} = 0.5 °C min^{-1} complete nitridation was reached but with an excess of N. It is clear that the synthesis parameters could be optimized.

Other syntheses were made by varying the final temperature (500 °C vs 700 °C) and the final isotherm (2 h vs. 24 h). The results are included in Table 6, Table A.2 and Figure A.14. Unfortunately, Mo was still present after holding the final temperature at 700 °C for 24 h (sample 5-T700-24). It is interesting to note that the amount of Mo_2N increased in detriment to metallic Mo. Moreover, the crystallite size of Mo increased for the sample 5-T700-24 (11 *vs.* 15 nm). It seems that the growth of Mo particles is a faster process than the nitridation, and could be the reason for incomplete nitridation for these samples synthesized at 700 °C (2 h and 24 h). This is consistent with what was observed during the formation of β-Mo_2N from Mo (Mo_2N-5-Mo and Mo_2N-0.5-Mo; Table A.1) where we could not reach full nitridation due to the growth of Mo particles.

As shown before, the reduction of MoO_3 takes place at lower temperatures for MoO_3 on support than for bulk MoO_3, therefore different samples were synthesized at 500 °C for 2 h. Despite the absence of Mo on the XRD patterns (Figure A.14), full nitridation was not reached for short isotherm (N = 0.14 wt%; Table 6). By prolonging the isotherm to 24 h, fully nitridated $Mo_2N_{0.96}$ was obtained (sample 5-T500-24; N = 0.65 wt%). Finally, a similar synthesis was conducted with lower temperature rate (sample 0.5-T500-24) and the nitridation was complete ($Mo_2N_{0.96}$, N = 0.65 wt%). At 500 °C, the

reduction/nitridation step did not affect the specific surface areas of the samples (46-49 m^2 g^{-1}). Therefore, the presence of TiO_2 allows to lower the temperature of synthesis of Mo_2N from 700 to 500 °C.

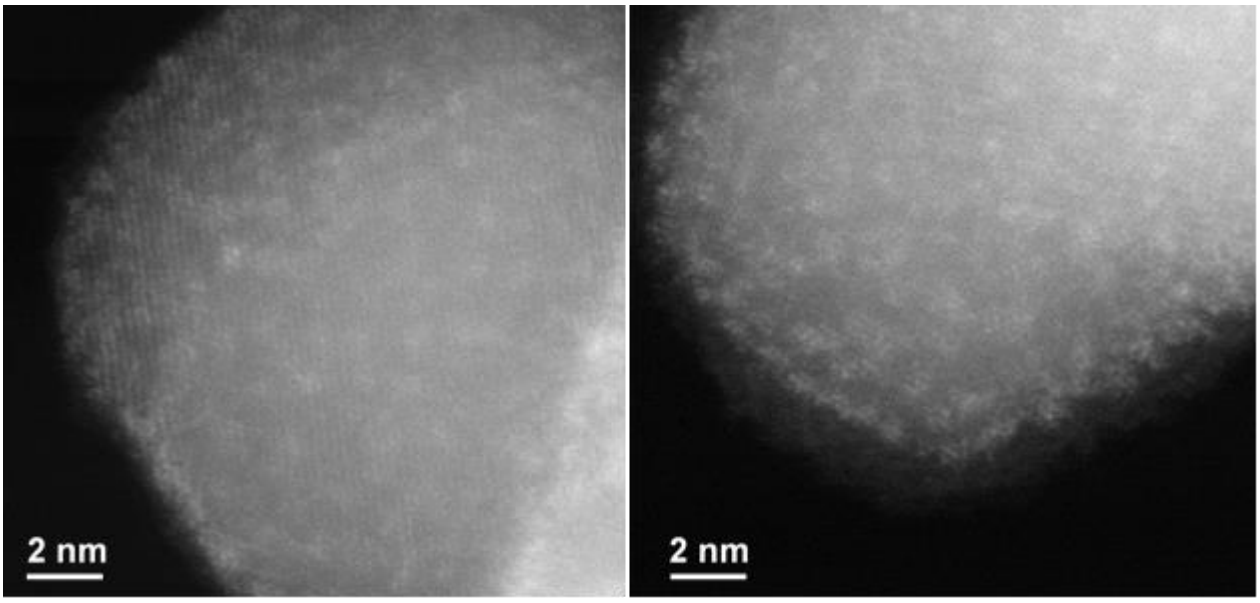

Figure 11. *Representative STEM-HAADF images of Mo_2N/TiO_2, sample 0.5-T500-24*

The dispersion of the nitride particles on the surface was then assessed by TEM and STEM. For Mo_2N/TiO_2, sample 5-T500-24 (Figure A.15 and A.16), the pictures present large particles (ca. 8-10 nm). The d-spacing and angles were estimated for some particles. The distances correspond to Mo_2N ($d_{(11-1)}$ = 0.243 nm and $d_{(200)}$ = 0.207 nm), however it was not possible to distinguish between tetragonal and cubic structures (Table A.3 and Table A.4). The STEM images associated with Mo_2N/TiO_2, sample 0.5-500°C-24h (Figure 11) present very well dispersed small clusters (< 0.5 nm). The presence of nitrogen was confirmed by EDX for both samples.

To conclude, Mo_2N/TiO_2 was successfully synthesized at 500 °C for 24 h. The heating rate seems to affect the dispersion, where small clusters were observed at 0.5 °C min^{-1}. Unfortunately, it is difficult to determine the crystallographic phase of Mo_2N.

Table 7. Influence of heating rate (T_{rate}), temperature maximal (T_{max}) and time of hold on Mo_2N/CeO_2 structural properties

Mo_2N/CeO_2 Synthesis condition: T_{rate}-T_{max}-iso	Composition and crystallite size (nm)[a]	S_{BET} (m^2 g^{-1})	N (wt%)[b]	Mo_2N_x (x)[b]
5-T700-2	Mo (14), Mo_2N (7)	34	-	-
5-T600-24	-	46	0.45	0.66
5-T500-24	-	-	0.24	0.35
0.5-T700-2	Mo_2N (3)	33	0.63	0.93
0.5-T600-24	-	48	0.37	0.55

[a] *composition and crystallite size based on XRD analyses*

[b] *based on elemental analyses*

Finally, the same methodology was applied to MoO_3/CeO_2. Figure A.12 shows diffractograms of CeO_2-supported molybdenum nitrides synthesized at 700 °C. A very small peak at 37.5 ° was observed and associated with the main plan of Mo_2N for both heating rates (0.5 and 5 °C min^{-1}). Other peaks of nitride phase could not be visible since they overlap with those of CeO_2. The presence of the metallic Mo (peak at 40.5 °) suggests incomplete nitridation when employing fast heating rate (5 °C min^{-1}), as in the case of Mo_2N/TiO_2. At lower heating rate, the nitrogen content (N = 0.63 wt%, Table 7) corresponds to $Mo_2N_{0,93}$. Some samples were synthesized at 500 °C and 600 °C, for 24 h (Table 7, Figure A.17). We could not observe any crystalline phase (beside CeO_2) by XRD, and the nitrogen contents suggest incomplete nitridation (N = 0.24-0.45 wt%).

These results reveal that supported molybdenum nitride can be synthesized at 500 °C on TiO_2, while 700 °C is required on CeO_2 for full nitridation. Low heating rate (0.5 °C min^{-1}) favor high degree of nitridation and high dispersion.

4. Conclusions

We propose a simple synthesis method of β and γ-Mo_2N bulk (and supported) materials by TPN of MoO_3 (MoO_3/support) with 15% v/v N_2/H_2 at 700 °C. By varying the parameters of synthesis, it is possible to tune the crystallographic phase of the nitride and the amount of nitrogen within the structure. Concentration of N-vacancies in bulk materials can be tuned by varying the GHSV, the final nitridation temperature and MoO_3-particle size. We have elucidated, for the first time, that formation mechanisms of both, β and γ, phases in N_2/H_2 systems pass through the same intermediate phases including: molybdenum bronze (H_xMoO_3), MoO_2 and Mo. We proved that the determining parameters, temperature rate and GHSV, impact the crystallite size of metallic Mo and the kinetic of the reduction and nitridation. For TiO_2 supported nitrides, pure Mo_2N phase is obtained at only 500 °C and control of N content can be achieved by adjusting the time of the final isotherm (T_{iso} = 2-24 h). Moreover very small clusters (< 0.5 nm) of Mo_2N are obtained on TiO_2. In the case of CeO_2 supported molybdenum nitrides complete nitridation is achieved at 700 °C with T_{rate} = 0.5 °C min^{-1}, while N-deficient materials are synthesized by lowering the T_{max}. Molybdenum nitride was synthesized in an XPS apparatus, after atomic liquid injection of the precursor, followed by oxidation and reduction/nitridation. The UPS data, coupled with DFT calculation, confirmed the *in situ* formation of β-Mo_2N and its metallic character.

Author Contributions

Original draft (A. Lilić, N. Perret), writing/review/editing (S. Loridant, C. Michel, L. Cardenas), visualization (A. Lilić, N. Perret, L. Cardenas), conceptualization/supervision (N. Perret, S. Loridant, C. Michel, P. Jame), validation (A. Lilić, E. Bonjour), software (A. Lilić, C. Michel), funding acquisition and resources (N. Perret, S. Loridant, C. Michel, P. Jame), project administration (N. Perret), formal analysis/investigation/methodology (A. Lilić, L. Cardenas, A. Mesbah, E. Bonjour).

Conflicts of interest

Theree are no conflicts to declare.

Acknowledgements

This work was supported by the Agence Nationale de la Recherche [project NITAMIN, grant number ANR-17-CE07-0026, 2017]. Scientific services of IRCELYON are greatly acknowledged for their contribution to the research.

References

[1] S.T. Oyama, Introduction to the chemistry of transition metal carbides and nitrides, in: S.T. Oyama (Ed.), The Chemistry of Transition Metal Carbides and Nitrides, Springer Netherlands, Dordrecht, 1996, pp. 1–27.

[2] S. T. Oyama, Crystal Structure and Chemical Reactivity of Transition Metal Carbides and Nitrides, J. Solid State Chem. 96 (1992) 442–445. https://doi.org/10.1016/S0022-4596(05)80279-8

[3] C.L. Bull, T. Kawashima, P.F. McMillan, D. Machon, O. Shebanova, D. Daisenberger, E. Soignard, E. Takayama-Muromachi, L.C. Chapon, Crystal structure and high-pressure properties of γ-Mo_2N determined by neutron powder diffraction and X-ray diffraction, J. Solid State Chem. 179 (2006) 1762–1767. https://doi.org/10.1016/j.jssc.2006.03.011.

[4] X. Zhu, D. Yue, C. Shang, M. Fan, B. Hou, Phase composition and tribological performance of molybdenum nitride coatings synthesized by IBAD, Surf. Coat. Technol. 228 (2013) S184–S189. https://doi.org/10.1016/j.surfcoat.2012.06.032.

[5] A. Gilewicz, B. Warcholinski, D. Murzynski, The properties of molybdenum nitride coatings obtained by cathodic arc evaporation, Surf. Coat. Technol. 236 (2013) 149–158. https://doi.org/10.1016/j.surfcoat.2013.09.005.

[6] I. Jauberteau, A. Bessaudou, R. Mayet, J. Cornette, J. Jauberteau, P. Carles, T. Merle-Méjean, Molybdenum Nitride Films: Crystal Structures, Synthesis, Mechanical, Electrical and Some Other Properties, Coatings. 5 (2015) 656–687. https://doi.org/10.3390/coatings5040656.

[7] A. Gomathi, A. Sundaresan, C.N.R. Rao, Nanoparticles of superconducting γ-Mo_2N and δ-MoN, J. Solid State Chem. 180 (2007) 291–295. https://doi.org/10.1016/j.jssc.2006.10.020.

[8] S. Yoon, K.-N. Jung, C.S. Jin, K.-H. Shin, Synthesis of nitrided MoO_2 and its application as anode materials for lithium-ion batteries, J. Alloys Compd. 536 (2012) 179–183. https://doi.org/10.1016/j.jallcom.2012.04.116.

[9] W.-F. Chen, J.T. Muckerman, E. Fujita, Recent developments in transition metal carbides and nitrides as hydrogen evolution electrocatalysts, Chem. Commun. 49 (2013) 8896–8909. https://doi.org/10.1039/c3cc44076a.

[10] X. Peng, C. Pi, X. Zhang, S. Li, K. Huo, P.K. Chu, Recent progress of transition metal nitrides for efficient electrocatalytic water splitting, Sustainable Energy Fuels. 3 (2019) 366–381. https://doi.org/10.1039/C8SE00525G.
[11] A.B. Dongil, Recent Progress on Transition Metal Nitrides Nanoparticles as Heterogeneous Catalysts, Nanomaterials. 9 (2019) 1111. https://doi.org/10.3390/nano9081111.
[12] Z. Lin, S.R. Denny, J.G. Chen, Transition metal carbides and nitrides as catalysts for thermochemical reactions, J. Catal. 404 (2021) 929–942. https://doi.org/10.1016/j.jcat.2021.06.022.
[13] F. Cárdenas-Lizana, D. Lamey, L. Kiwi-Minsker, M.A. Keane, Molybdenum nitrides: a study of synthesis variables and catalytic performance in acetylene hydrogenation, J. Mater. Sci. 53 (2018) 6707–6718. https://doi.org/10.1007/s10853-018-2009-x.
[14] N. Perret, D. Lamey, L. Kiwi-Minsker, F. Cárdenas-Lizana, M.A. Keane, New insights into the effect of nitrogen incorporation in Mo: catalytic hydrogenation *vs.* hydrogenolysis, Catal. Sci. Technol. 9 (2019) 1891–1901. https://doi.org/10.1039/C9CY00216B.
[15] Z. Li, C. Chen, E. Zhan, N. Ta, W. Shen, Mo_2N nanobelts for dehydrogenation of aromatic alcohols, Catal. Commun. 51 (2014) 58–62. https://doi.org/10.1016/j.catcom.2014.03.029.
[16] M. Nagai, Y. Goto, A. Miyata, M. Kiyoshi, K. Hada, K. Oshikawa, S. Omi, Temperature-Programmed Reduction and XRD Studies of Ammonia-Treated Molybdenum Oxide and Its Activity for Carbazole Hydrodenitrogenation, J. Catal. 182 (1999) 292–301. https://doi.org/10.1006/jcat.1998.2365.
[17] N. Perret, F. Cárdenas-Lizana, D. Lamey, V. Laporte, L. Kiwi-Minsker, M.A. Keane, Effect of Crystallographic Phase (β vs. γ) and Surface Area on Gas Phase Nitroarene Hydrogenation Over Mo_2N and Au/Mo_2N, Top. Catal. 55 (2012) 955–968. https://doi.org/10.1007/s11244-012-9881-4.
[18] I.T. Ghampson, C. Sepúlveda, R. Garcia, J.L. García Fierro, N. Escalona, W.J. DeSisto, Comparison of alumina- and SBA-15-supported molybdenum nitride catalysts for hydrodeoxygenation of guaiacol, Appl. Catal., A 435–436 (2012) 51–60. https://doi.org/10.1016/j.apcata.2012.05.039.
[19] C.W. Colling, L.T. Thompson, The structure and function of supported molybdenum nitride hydrodenitrogenation catalysts, J. Catal. 146 (1994) 193–203. http://dx.doi.org/10.1016/0021-9517(94)90022-1
[20] I.T. Ghampson, C. Sepúlveda, R. Garcia, L.R. Radovic, J.L.G. Fierro, W.J. DeSisto, N. Escalona, Hydrodeoxygenation of guaiacol over carbon-supported molybdenum nitride catalysts: Effects of nitriding methods and support properties, Appl. Catal., A 439–440 (2012) 111–124. https://doi.org/10.1016/j.apcata.2012.06.047.
[21] E. Markel, Catalytic hydrodesulfurization by molybdenum nitride, J. Catal. 126 (1990) 643–657. https://doi.org/10.1016/0021-9517(90)90027-H.
[22] Y. Zhang, Z. Wei, W. Yan, P. Ying, C. Ji, X. Li, Z. Zhou, X. Sun, Q. Xin, Synthesis and hydrodesulfurization (HDS) and hydrogenation (HYD) activity of dimolybdenum nitride, Catal. Today. 30 (1996) 135–139. https://doi.org/10.1016/0920-5861(96)00003-X.
[23] K.R. McCrea, J.W. Logan, T.L. Tarbuck, J.L. Heiser, M.E. Bussell, Thiophene Hydrodesulfurization over Alumina-Supported Molybdenum Carbide and Nitride Catalysts: Effect of Mo Loading and Phase, J. Catal. 171 (1997) 255–267. https://doi.org/10.1006/jcat.1997.1805.
[24] M. Nagai, Y. Goto, H. Ishii, S. Omi, XPS and TPSR study of nitrided molybdena–alumina catalyst for the hydrodesulfurization of dibenzothiophene, Appl. Catal., A 192 (2000) 189–199. https://doi.org/10.1016/S0926-860X(99)00341-5.
[25] I.T. Ghampson, C. Sepúlveda, R. Garcia, B.G. Frederick, M.C. Wheeler, N. Escalona, W.J. DeSisto, Guaiacol transformation over unsupported molybdenum-based nitride catalysts, Appl. Catal., A 413–414 (2012) 78–84. https://doi.org/10.1016/j.apcata.2011.10.050.

[26] M. Nagai, T. Miyao, T. Tuboi, Hydrodesulfurization of dibenzothiophene on alumina-supported molybdenum nitride, Catal. Lett. 18 (1993) 9–14. https://doi.org/10.1007/BF00769493.
[27] J. Trawczyński, Effect of synthesis conditions on the molybdenum nitride catalytic activity, Catal. Today. 65 (2001) 343–348. https://doi.org/10.1016/S0920-5861(00)00563-0.
[28] R.C.V. McGee, L.T. Thompson, Nature of acid-base sites on molybdenum nitride catalysts: Effect of nitrogen and oxygen content, Appl. Catal., A 605 (2020) 117777. https://doi.org/10.1016/j.apcata.2020.117777.
[29] R.S. Wise, E.J. Markel, Catalytic NH_3 decomposition by topotactic molybdenum oxides and nitrides: Effect on temperature programmed gamma-Mo_2N synthesis, J. Catal. 145 (1994) 335–343. https://doi.org/10.1006/jcat.1994.1042
[30] R.S. Wise, E.J. Markel, Synthesis of high surface area molybdenum nitride in mixtures of nitrogen and hydrogen, J. Catal. 145 (1994) 344–355. https://doi.org/10.1006/jcat.1994.1043
[31] S. Li, W.B. Kim, J.L. Lee, Effect of the reactive gas on the solid-state transformation of molybdenum trioxide to carbides and nitrides, Chem Mater. 10 (1998) 1853–1862. https://doi-org/10.1021/cm9800229
[32] A.G. Cairns, J.G. Gallagher, J.S.J. Hargreaves, D. Mckay, E. Morrison, J.L. Rico, K. Wilson, The influence of precursor source and thermal parameters upon the formation of beta-phase molybdenum nitride, J. Alloys Compd. 479 (2009) 851–854. https://doi.org/10.1016/j.jallcom.2009.01.065.
[33] S. Gong, H. Chen, W. Li, B. Li, Synthesis of β-$Mo_2N_{0.78}$ hydrodesulfurization catalyst in mixtures of nitrogen and hydrogen, Appl. Catal., A 279 (2005) 257–261. https://doi.org/10.1016/j.apcata.2004.10.038.
[34] F. Cárdenas-Lizana, S. Gómez-Quero, N. Perret, L. Kiwi-Minsker, M.A. Keane, β-Molybdenum nitride: synthesis mechanism and catalytic response in the gas phase hydrogenation of p-chloronitrobenzene, Catal. Sci. Technol. 1 (2011) 794–801. https://doi.org/10.1039/c0cy00011f.
[35] S.W. Gong, H.K. Chen, W. Li, B.Q. Li, Catalytic Behaviors of β-$Mo_2N_{0.78}$ as a Hydrodesulfurization Catalyst, Energy Fuels. 20 (2006) 1372–1376. https://doi.org/10.1021/ef050208b.
[36] A.G. Cairns, J.G. Gallagher, J.S.J. Hargreaves, D. Mckay, J.L. Rico, K. Wilson, The effect of low levels of dopants upon the formation and properties of beta-phase molybdenum nitride, J. Solid State Chem. 183 (2010) 613–619. https://doi.org/10.1016/j.jssc.2009.12.018.
[37] L. Volpe, M. Boudart, Compounds of molybdenum and tungsten with high specific surface area. 1. nitrides, J. Solid State Chem. 59 (1985) 332–347. https://doi.org/10.1016/0022-4596(85)90301-9.
[38] M.E. Kreider, M.B. Stevens, Y. Liu, A.M. Patel, M.J. Statt, B.M. Gibbons, A. Gallo, M. Ben-Naim, A. Mehta, R.C. Davis, A.V. Ievlev, J.K. Nørskov, R. Sinclair, L.A. King, T.F. Jaramillo, Nitride or Oxynitride? Elucidating the Composition–Activity Relationships in Molybdenum Nitride Electrocatalysts for the Oxygen Reduction Reaction, Chem. Mater. 32 (2020) 2946–2960. https://doi.org/10.1021/acs.chemmater.9b05212.
[39] Y. Zheng, D. Chen, X. Zhu, Aromatic hydrocarbon production by the online catalytic cracking of lignin fast pyrolysis vapors using Mo_2N/γ-Al_2O_3, J. Anal. Appl. Pyrolysis. 104 (2013) 514–520. https://doi.org/10.1016/j.jaap.2013.05.018.
[40] S. Gong, H. Chen, W. Li, B. Li, Thiophene hydrodesulfurization over alumina-supported β-$Mo_2N_{0.78}$ catalyst, Catal. Commun. 5 (2004) 621–624. https://doi.org/10.1016/j.catcom.2004.07.012.
[41] X. Li, Z. Zhang, V.E. Henrich, Inelastic electron background function for ultraviolet photoelectron spectra, J. Electron Spectrosc. Relat. Phenom. 63 (1993) 253–265. https://doi.org/10.1016/0368-2048(93)87007-M.

[42] C. Maheu, L. Cardenas, E. Puzenat, P. Afanasiev, C. Geantet, UPS and UV spectroscopies combined to position the energy levels of TiO_2 anatase and rutile nanopowders, Phys. Chem. Chem. Phys. 20 (2018) 25629–25637. https://doi.org/10.1039/C8CP04614J.
[43] J.P. Perdew, K. Burke, M. Ernzerhof, Generalized Gradient Approximation Made Simple, Phys. Rev. Lett. 77 (1996) 3865–3868. https://doi.org/10.1103/PhysRevLett.77.3865.
[44] G. Kresse, J. Furthmüller, Efficiency of ab-initio total energy calculations for metals and semiconductors using a plane-wave basis set, Comput. Mater. Sci. 6 (1996) 15–50. https://doi.org/10.1016/0927-0256(96)00008-0.
[45] G. Kresse, J. Furthmüller, Efficient iterative schemes for *ab initio* total-energy calculations using a plane-wave basis set, Phys. Rev. B. 54 (1996) 11169–11186. https://doi.org/10.1103/PhysRevB.54.11169.
[46] P.E. Blöchl, Projector augmented-wave method, Phys. Rev. B. 50 (1994) 17953–17979. https://doi.org/10.1103/PhysRevB.50.17953.
[47] G. Kresse, D. Joubert, From ultrasoft pseudopotentials to the projector augmented-wave method, Phys. Rev. B. 59 (1999) 1758–1775. https://doi.org/10.1103/PhysRevB.59.1758.
[48] H.J. Monkhorst, J.D. Pack, Special points for Brillouin-zone integrations, Phys. Rev. B. 13 (1976) 5188–5192. https://doi.org/10.1103/PhysRevB.13.5188.
[49] H.S. Abdelkader, A. Rabahi, M. Benaissa, M.K. Benabadji, Theoretical investigation of structural and mechanical stability of Mo_2N, Solid State Commun. 314–315 (2020) 113919. https://doi.org/10.1016/j.ssc.2020.113919.
[50] L.-P. Ding, P. Shao, F.-H. Zhang, C. Lu, X.-F. Huang, Prediction of Molybdenum Nitride from First-Principle Calculations: Crystal Structures, Electronic Properties, and Hardness, J. Phys. Chem. C. 122 (2018) 21039–21046. https://doi.org/10.1021/acs.jpcc.8b04779.
[51] D.O. Scanlon, G.W. Watson, D.J. Payne, G.R. Atkinson, R.G. Egdell, D.S.L. Law, Theoretical and Experimental Study of the Electronic Structures of MoO_3 and MoO_2, J. Phys. Chem. C. 114 (2010) 4636–4645. https://doi.org/10.1021/jp9093172.
[52] K. Inzani, T. Grande, F. Vullum-Bruer, S.M. Selbach, A van der Waals Density Functional Study of MoO_3 and Its Oxygen Vacancies, J. Phys. Chem. C. 120 (2016) 8959–8968. https://doi.org/10.1021/acs.jpcc.6b00585.
[53] A. J Jackson, A. M Ganose, A. Regoutz, R. G. Egdell, D. O Scanlon, Galore: Broadening and weighting for simulation of photoelectron spectroscopy, J. Open Source Softw. 3 (2018) 773. https://doi.org/10.21105/joss.00773.
[54] J.J. Yeh, I. Lindau, Atomic Subshell Photoionization Cross Sections and Asymmetry Parameters: $1 \leq Z \leq 103$, At. Data Nucl. Data Tables. 32 (1985) 1–155. https://doi.org/10.1016/0092-640X(85)90016-6
[55] J.S.J. Hargreaves, Heterogeneous catalysis with metal nitrides, Coord. Chem. Rev. 257 (2013) 2015–2031. https://doi.org/10.1016/j.ccr.2012.10.005.
[56] L. Kong, J. Wu, B. Lü, Q. Li, T. Xiong, Midscale Preparation and Characterization of Transient Metal Nitride Catalyst, Ind. Eng. Chem. Res. 47 (2008) 1779–1783. https://doi.org/10.1021/ie070829n.
[57] Z. Wei, Q. Xin, P. Grange, B. Delmon, TPD and TPR Studies of Molybdenum Nitride, J. Catal. 168 (1997) 176–182. https://doi.org/10.1006/jcat.1997.1641
[58] M. Nagai, Y. Goto, O. Uchino, S. Omi, TPD and XRD studies of molybdenum nitride and its activity for hydrodenitrogenation of carbazole, Catal. Today. 43 (1998) 249–259. https://doi.org/10.1016/S0920-5861(98)00154-0.
[59] H. Jehn, P. Ettmayer, The molybdenum-nitrogen phase diagram, J. Less-Common Met. 58 (1978) 85–98. https://doi.org/10.1016/0022-5088(78)90073-5.
[60] Y.-J. Zhang, Q. Xin, I. Rodriguez-Ramos, A. Guerrero-Ruiz, Simultaneous hydrodesulfurization of thiophene and hydrogenation of cyclohexene over dimolybdenum nitride catalysts, Appl. Catal., A 180 (1999) 237–245. https://doi.org/10.1016/S0926-860X(98)00370-6.

[61] T. Matsuda, Y. Hirata, H. Itoh, H. Sakagami, N. Takahashi, Effect of Reduction Temperature on the Transformation of MoO_3 to MoO_x with a Large Surface Area, Microporous Mesoporous Mater. 42 (2001) 337–344. https://doi.org/10.1016/S1387-1811(00)00342-5
[62] J. Choi, R. Curl, L. Thompson, Molybdenum nitride catalysts I. Influence of the synthesis factors on structural properties, J. Catal. 146 (1994) 218–227. https://doi.org/10.1016/0021-9517(94)90025-6.
[63] A. Chithambararaj, D. Bhagya Mathi, N. Rajeswari Yogamalar, A. Chandra Bose, Structural Evolution and Phase Transition of $[NH_4]_6Mo_7O_{24}.4H_2O$ to 2D Layered MoO_{3-x}, Mater. Res. Express. 2 (2015) 055004. https://doi.org/10.1088/2053-1591/2/5/055004.
[64] C.H. Jaggers, J.N. Michaels, A.M. Stacy, Preparation of high-surface-area transition-metal nitrides: molybdenum nitrides, Mo_2N and MoN, Chem. Mater. 2 (1990) 150–157. https://doi.org/10.1021/cm00008a015.
[65] J. Monnier, H. Sulimma, A. Dalai, G. Caravaggio, Hydrodeoxygenation of oleic acid and canola oil over alumina-supported metal nitrides, Appl. Catal., A 382 (2010) 176–180. https://doi.org/10.1016/j.apcata.2010.04.035.
[66] H. Zhong, H. Zhang, G. Liu, Y. Liang, J. Hu, B. Yi, A novel non-noble electrocatalyst for PEM fuel cell based on molybdenum nitride, Electrochem. Commun. 8 (2006) 707–712. https://doi.org/10.1016/j.elecom.2006.02.020.
[67] S.L. Roberson, D. Finello, R.F. Davis, Synthesis of low oxygen concentration molybdenum nitride films, Mater. Sci. Eng., A 248 (1998) 198–205. https://doi.org/10.1016/S0921-5093(98)00483-3.
[68] J. Barbosa, L. Cunha, L. Rebouta, C. Moura, F. Vaz, S. Carvalho, E. Alves, E. Le Bourhis, Ph. Goudeau, J.P. Rivière, Properties of MoN_xO_y thin films as a function of the N/O ratio, Thin Solid Films. 494 (2006) 201–206. https://doi.org/10.1016/j.tsf.2005.07.192.
[69] P. Delporte, F. Meunier, C. Pham-Huu, P. Vennegues, M.J. Ledoux, J. Guille, Physical characterization of molybdenum oxycarbide catalyst; TEM, XRD and XPS, Catal. Today. 23 (1995) 251–267. https://doi.org/10.1016/0920-5861(94)00166-Y.
[70] R.J. Cava, R.S. Roth, T. Siegrist, B. Hessen, J.J. Krajewski, W.F. Peck, $Cs_{8.5}W_{15}O_{48}$ and CsW_2O_6: Members of a New Homologous Series of Cesium Tungsten Oxides, J. Solid State Chem. 103 (1993) 359–365. https://doi.org/10.1006/jssc.1993.1111.
[71] V. Luca, E. Drabarek, H. Chronis, T. McLeod, Tungsten Bronze-Based Nuclear Waste Form Ceramics. Part 3: The System $Cs_{0.3}M_xW_{1-x}O_3$ for the Immobilization of Radio Cesium, J. Nucl. Mater. 358 (2006) 164–175. https://doi.org/10.1016/j.jnucmat.2006.06.019.
[72] K. Eda, Raman Spectra of Hydrogen Molybdenum Bronze, $H_{0.30}MoO_z$, J. Solid State Chem. 98 (1992) 350–357. https://doi.org/10.1016/S0022-4596(05)80245-2
[73] L. Seguin, M. Figlarz, R. Cavagnat, J.-C. Lassègues, Infrared and Raman Spectra of MoO_3 Molybdenum Trioxides and $MoO_3 \cdot xH_2O$ Molybdenum Trioxide Hydrates, Spectrochim. Acta. A. Mol. Biomol. Spectrochimica Acta. A 51 (1995) 1323–1344. https://doi.org/10.1016/0584-8539(94)00247-9.
[74] M.A. Camacho-López, L. Escobar-Alarcón, M. Picquart, R. Arroyo, G. Córdoba, E. Haro-Poniatowski, Micro-Raman study of the m-MoO_2 to α-MoO_3 transformation induced by cw-laser irradiation, Opt. Mater. 33 (2011) 480–484. https://doi.org/10.1016/j.optmat.2010.10.028.
[75] G. Mestl, In situ Raman spectroscopy for the characterization of MoVW mixed oxide catalysts, J. Raman Spectrosc. 33 (2002) 333–347. https://doi.org/10.1002/jrs.843.
[76] J.Z. Ou, J.L. Campbell, D. Yao, W. Wlodarski, K. Kalantar-zadeh, In Situ Raman Spectroscopy of H_2 Gas Interaction with Layered MoO_3, J. Phys. Chem. C. 115 (2011) 10757–10763. https://doi.org/10.1021/jp202123a.
[77] M. Šetka, R. Calavia, L. Vojkůvka, E. Llobet, J. Drbohlavová, S. Vallejos, Raman and XPS studies of ammonia sensitive polypyrrole nanorods and nanoparticles, Scientific Reports 9 (2019) 8465. https://doi.org/10.1038/s41598-019-44900-1.

[78] J. Baltrusaitis, B. Mendoza-Sanchez, V. Fernandez, R. Veenstra, N. Dukstiene, A. Roberts, N. Fairley, Generalized molybdenum oxide surface chemical state XPS determination via informed amorphous sample model, Appl. Surf. Sci. 326 (2015) 151–161. https://doi.org/10.1016/j.apsusc.2014.11.077.
[79] M.T. Greiner, L. Chai, M.G. Helander, W.-M. Tang, Z.-H. Lu, Metal/Metal-Oxide Interfaces: How Metal Contacts Affect the Work Function and Band Structure of MoO_3, Adv. Funct. Mater. 23 (2013) 215–226. https://doi.org/10.1002/adfm.201200993.
[80] M.B. Kanoun, S. Goumri-Said, M. Jaouen, Structure and mechanical stability of molybdenum nitrides: A first-principles study, Phys. Rev. B. 76 (2007) 134109. https://doi.org/10.1103/PhysRevB.76.134109.
[81] A. Shrestha, X. Gao, J.C. Hicks, C. Paolucci, Nanoparticle Size Effects on Phase Stability for Molybdenum and Tungsten Carbides, Chem. Mater. 33 (2021) 4606–4620. https://doi.org/10.1021/acs.chemmater.1c01120.
[82] Z. Tišler, R. Velvarská, L. Skuhrovcová, L. Pelíšková, U. Akhmetzyanova, Key Role of Precursor Nature in Phase Composition of Supported Molybdenum Carbides and Nitrides, Materials. 12 (2019) 415. https://doi.org/10.3390/ma12030415.
[83] Y. Lee, T. H. Nguyen, A. Khodakov, A. A. Adesina, Physicochemical attributes of oxide supported Mo_2N catalysts synthesised via sulphide nitridation, J. Mol. Catal. Chem. 211 (2004) 191–197. https://doi.org/10.1016/j.molcata.2003.10.008.
[84] L. Stagi, C.M. Carbonaro, R. Corpino, D. Chiriu, P.C. Ricci, Light Induced TiO_2 Phase Transformation: Correlation with Luminescent Surface Defects: Light Induced TiO_2 Phase Transformation, Phys. Status Solidi B. 252 (2015) 124–129. https://doi.org/10.1002/pssb.201400080.
[85] R. Murugan, H. Chang, Thermo-Raman Investigations on Thermal Decomposition of $(NH_4)_6Mo_7O_{24}\cdot 4H_2O$, J. Chem. Soc., Dalton Trans. (2001) 3125. https://doi.org/10.1039/b102959m.
[86] M. Shetty, K. Murugappan, T. Prasomsri, W.H. Green, Y. Román-Leshkov, Reactivity and stability investigation of supported molybdenum oxide catalysts for the hydrodeoxygenation (HDO) of m-cresol, J. Catal. 331 (2015) 86–97. https://doi.org/10.1016/j.jcat.2015.07.034.
[87] S. Loridant, Raman spectroscopy as a powerful tool to characterize ceria-based catalysts, Catal. Today. 373 (2021) 98–111. https://doi.org/10.1016/j.cattod.2020.03.044.
[88] H. Hu, I.E. Wachs, S.R. Bare, Surface Structures of Supported Molybdenum Oxide Catalysts: Characterization by Raman and Mo L3-Edge XANES, J. Phys. Chem. 99 (1995) 10897–10910. https://doi.org/10.1021/j100027a034.
[89] S. Boullosa-Eiras, R. Lødeng, H. Bergem, M. Stöcker, L. Hannevold, E.A. Blekkan, Catalytic hydrodeoxygenation (HDO) of phenol over supported molybdenum carbide, nitride, phosphide and oxide catalysts, Catal. Today. 223 (2014) 44–53. https://doi.org/10.1016/j.cattod.2013.09.044.
[90] B.-W. Wang, Y.-Q. Yao, S.-H. Liu, Z.-Y. Hu, Z.-H. Li, X.-B. Ma, Effects of MoO_3 loading and calcination temperature on the catalytic performance of MoO_3/CeO_2 toward sulfur-resistant methanation, Fuel Process. Technol. 138 (2015) 263–270. https://doi.org/10.1016/j.fuproc.2015.06.009.
[91] D.A.H. Hanaor, C.C. Sorrell, Review of the anatase to rutile phase transformation, J. Mater. Sci. 46 (2011) 855–874. https://doi.org/10.1007/s10853-010-5113-0.
[92] M. Abou Hamdan, S. Loridant, M. Jahjah, C. Pinel, N. Perret, TiO_2-supported molybdenum carbide: An active catalyst for the aqueous phase hydrogenation of succinic acid, Appl. Catal., A 571 (2019) 71–81. https://doi.org/10.1016/j.apcata.2018.11.009.